

Stieltjes Functions and Spectral Analysis in the Physics of Sea Ice

Kenneth M. Golden, N. Benjamin Murphy, and Elena Cherkaev

Department of Mathematics, University of Utah
155 S 1400 E RM 233, Salt Lake City, UT 84112-0090

October 15, 2022

Abstract

Polar sea ice is a critical component of Earth's climate system. As a material it is a multiscale composite with temperature dependent millimeter-scale brine microstructure, and centimeter-scale polycrystalline microstructure which is largely determined by how the ice was formed. The surface layer of the polar oceans can be viewed as a granular composite of ice floes in a sea water host, with floe sizes ranging from centimeters to tens of kilometers. A principal challenge in modeling sea ice and its role in climate is how to use information on smaller scale structure to find the effective or homogenized properties on larger scales relevant to process studies and coarse-grained climate models. That is, how do you predict macroscopic behavior from microscopic laws, like in statistical mechanics and solid state physics? Also of great interest in climate science is the inverse problem of recovering parameters controlling small scale processes from large scale observations. Motivated by sea ice remote sensing, the analytic continuation method for obtaining rigorous bounds on the homogenized coefficients of two phase composites was applied to the complex permittivity of sea ice, which is a Stieltjes function of the ratio of the permittivities of ice and brine. Integral representations for the effective parameters distill the complexities of the composite microgeometry into the spectral properties of a self-adjoint operator like the Hamiltonian in quantum physics. These techniques have been extended to polycrystalline materials, advection diffusion processes, and ocean waves in the sea ice cover. Here we discuss this powerful approach in homogenization, highlighting the spectral representations and resolvent structure of the fields that are shared by the two component theory and its extensions. Spectral analysis of sea ice structures leads to a random matrix theory picture of percolation processes in composites, establishing parallels to Anderson localization and semiconductor physics, which then provides new insights into the physics of sea ice.

1 Introduction

The precipitous loss of nearly half the extent of the summer Arctic sea ice cover over the past four decades or so, since satellite observations started in 1979, is perhaps one of the most visible large-scale changes on Earth's surface connected to planetary warming, with significant implications for the Arctic and beyond [129, 130, 95, 113, 114]. While the response of the sea ice pack surrounding the Antarctic continent to the changing climate has perhaps not been as clear as in the Arctic, this past year the summer sea ice extent set a record low [138]. The emerging dynamics of Earth's polar marine environments are complex and highly variable. Yet they are increasingly important to understand and predict, as the sea ice packs form a key component of the climate system, are

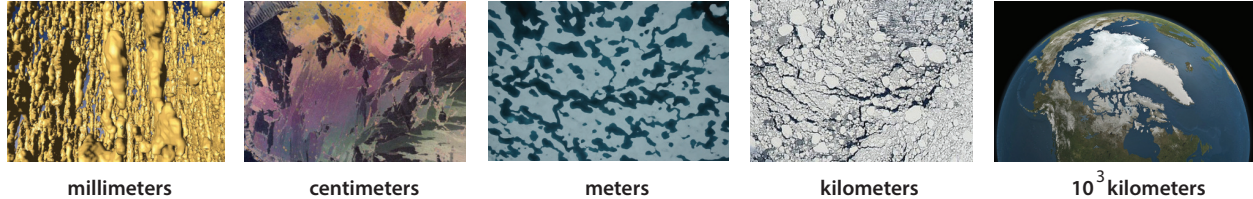


Figure 1: **Sea ice as a multiscale composite material.** From left to right: millimeter-scale brine inclusions that form the porous microstructure of sea ice [69]; centimeter-scale polycrystalline structure of sea ice [2]; melt ponds on Arctic sea ice in late spring and summer (D. Perovich) turn the surface into a two phase composite of ice and melt water; the sea ice pack as a granular composite viewed from space (NASA), with “grains” ranging in horizontal extent from meters to tens of kilometers; the Arctic Ocean viewed from space (NASA).

indicators of our changing climate, and directly impact expanding human activities in these regions. Sea ice has bearing on almost any study of the physics or biology of the polar marine system, as well as on almost any maritime operations or logistics. Advancing our ability to analyze, model, and predict the behavior of sea ice is critical to improving projections of climate change and the response of polar ecosystems, and in meeting the challenges of increased human activities in the Arctic [66].

One of the fascinating, yet challenging aspects of modeling sea ice and its role in global climate is the sheer range of relevant length scales — over ten orders of magnitude, from the sub-millimeter scale to thousands of kilometers, as indicated in Figure 1. Modeling the macroscopic behavior of sea ice on scales appropriate for climate models or for process studies depends on understanding the properties of sea ice on finer scales, down to individual floes and even the scale of the brine inclusions which control so many of the distinct physical characteristics of sea ice as a material. Climate models challenge the most powerful supercomputers to their fullest capacity. However, even the largest computers still limit the resolution to tens of kilometers and typically require clever approximations and parameterizations to incorporate the basic physics of sea ice [66, 63, 62]. One of the fundamental challenges in modeling sea ice—and a central theme in what follows—is how to account for the influence of the microscale on macroscopic behavior, that is, how to rigorously use information about smaller scales to predict effective behavior on larger scales. Here we consider three different homogenization problems in the physics of sea ice: the classic two phase problem of brine inclusions in an ice host, sea ice as a polycrystalline material, and advection diffusion processes such as thermal conduction or nutrient diffusion in the presence of, e.g. convective brine flow. All of these questions are also of particular interest in polar microbial ecology [134, 121].

We observe that this central problem of studying the effective properties of sea ice is analogous to the main focus of statistical mechanics where knowledge of molecular interactions or microscopic laws is used to find collective or macroscopic behavior [135, 36]. Moreover, it also shares fundamental similarities with homogenization theory for composites where larger scale effective properties are calculated from knowledge of the microstructure [102, 136, 10, 116, 86]. These fields of physics and applied mathematics provide a natural framework for treating sea ice in predictive models of climate, and improving projections of how Earth’s polar ice packs may evolve in the future.

The analytic continuation method (ACM) [12, 100, 56, 60, 102] in particular, yields powerful integral representations for the effective or homogenized transport coefficients of two component [56] or multicomponent [57, 53] media. The method exploits the properties of these coefficients as analytic functions of ratios of the constituent parameters for two phase media, such as the ratio of the electrical or thermal conductivities, or the complex permittivities. The geometry of

the composite microstructure is encoded into a self-adjoint operator G through the characteristic function which takes the values 1 in one component (brine) and 0 in the other (ice). The key step in obtaining the integral representation, say in the case of electrical conductivity, is to derive a formula for the local electric field in terms of the resolvent of G , and then apply the spectral theorem in an appropriate Hilbert space. This representation for the effective conductivity (or effective complex permittivity) achieves a complete separation between the component parameters in the variable, and the geometry of the microstructure embedded in the *spectral measure* of G , the principal mathematical object in the integral. In a discrete model of a composite, the operator G becomes a random matrix, whose eigenvalues and eigenvectors can be used to compute the spectral measure [108].

The Stieltjes or Herglotz structure of the effective parameters and their integral representations can be exploited to use the moments of the spectral measure, or the correlation functions of the composite microstructure, to find rigorous bounds on the homogenized transport coefficients [12, 100, 56, 53, 7, 102]. Bounds on the complex permittivity of sea ice as a two phase composite were first obtained in the context of remote sensing and the mathematical analysis of sea ice electromagnetic properties [55, 68, 67]. For example, the mass of the spectral measure is the brine volume fraction. If this is known, then one can obtain *elementary bounds* in the complex case, which reduce to the classical arithmetic and harmonic mean bounds for real parameters. If the material is further assumed to be statistically isotropic, then tighter Hashin-Shtrikman bounds can be obtained. Even tighter bounds can be obtained when the composite is assumed to have *matrix-particle* structure, such as separated brine inclusions in a pure ice host [23, 60], which leads to gaps in the spectrum of G , and tighter constraints on the support of the spectral measure. In remote sensing the inverse homogenization problem where knowledge of bulk electromagnetic behavior, such as measurements of the effective complex permittivity, is inverted to obtain bounds on the microstructural characteristics such as the brine volume fraction [32, 67, 74] and connectivity [115]. The *microscale* structure, which determines the spectral measure and the homogenized coefficient, is thus linked to the *macroscopic* behavior via the operator G and its spectral characteristics, and *vice versa*. In the multicomponent case with three or more constituents, the homogenized transport coefficients are analytic functions of two or more complex variables, and a polydisc representation formula was exploited to obtain bounds [57, 53].

The first area of application where the ACM was extended beyond the classical case of two component and multiphase composites is diffusive transport in the presence of a flow field, which is widely encountered throughout science and engineering [96, 17, 49, 50, 117, 93, 94, 147]. In addition to thermal, saline, and nutrient transport through the porous microstructure of sea ice, large scale transport of ice floes and heat are also advection diffusion processes. Avellaneda and Majda [3, 4] found a Stieltjes integral representation for the effective diffusivity as a function of the Péclet number for diffusion in an incompressible velocity field. Based on the approach in [56], they set up a Hilbert space framework and applied the spectral theorem to a resolvent representation involving analogues of G and the electric field, where the spectral measure depends on the geometry of the velocity field, and knowledge of its moments yields bounds on the effective diffusivity. In [110, 111] we proved novel versions of the Stieltjes formulas, developed a framework to numerically compute the spectral measures and a systematic method to find its moments – and thus a hierarchy of bounds, for both the time dependent and independent cases.

In another extension of the ACM to a large class of media, a Stieltjes integral representation and rigorous bounds for the effective complex permittivity of polycrystalline media were developed in [75], based on a resolvent formula for the electric field, and earlier observations in [101, 14, 102]. The bounds assume knowledge of the average crystal orientation and the complex permittivity tensor of an individual crystal grain. In sea ice, finding the complex permittivity tensor of an individual crys-

tal involves homogenizing the smaller scale brine microstructure [75]. The polycrystalline structure of sea ice, as characterized by the statistics of grain size, shape, and orientation, is influenced by the conditions under which the ice was grown [144, 119, 139]. For example, while sea ice grown in quiescent conditions tends to have rather large-grained *columnar* structure, when grown in more turbulent or wavy conditions it typically has a fine-grained *granular* structure. These distinctly different ice types have quite different fluid flow properties [65, 71]. Also, when there is a well-defined current direction during formation, crystal orientations tend to be statistically anisotropic within the horizontal plane [145], which can significantly affect the sea ice radar signature, and measurements of sea ice thickness and properties used to validate climate models [64, 97].

The interaction of ocean surface waves with polar sea ice is a critical process in Earth’s climate system; its accurate representation is of great importance for developing efficient climate models. Ice-ocean interactions have become increasingly important in the Arctic with the precipitous declines of summer sea ice extent and increases in wave activity [141], while at the same time the marginal ice zone (MIZ), which is characterized by strong wave-ice and atmosphere-ice-ocean interactions, has widened significantly [131]. These recent changes can have complex implications for both sea ice formation and melting [90]. Indeed, the propagation of surface waves through Earth’s sea ice covers is a complex phenomenon that drives their growth and decay. One of the main approaches to studying waves in sea ice which is valid when wavelengths are much greater than floe sizes, is to model the surface layer of the ice-covered ocean as a continuum with effective properties [9, 84, 140, 106]. Recently this fundamental problem in sea ice physics was homogenized, with a Stieltjes representation for the effective complex viscoelasticity of the surface layer, based on a resolvent formula for the local strain field. The integral involves a spectral measure of a self-adjoint operator depending on the geometry of the floe configurations. If its mass, or ice concentration, is known then rigorous bounds on the complex viscoelasticity are obtained in [124]. Previously this effective parameter had only been fitted to wave data. We will leave any detailed discussion of waves in sea ice to other publications.

Early on in our work in extending the ACM to the above problems in sea ice physics, it was clear that the classical approach based on bounding effective parameters using the moments of the spectral measure would in many cases have limited effectiveness. Bounds with only a moment or two known can be quite wide, particularly for a high contrast in the properties of the constituents, like in sea ice. We then developed a framework in the classic two phase case for computing the spectral measure through discretization of the relevant microstructures and finding the eigenvalues and eigenvectors of the matrix representation of G . By developing the mathematical foundation for these computations [108] and studying the properties of computed spectral measures for a broad range of sea ice and other microstructures, like human bone [70], we discovered that the statistics of the eigenvalues displayed fascinating behavior depending on the connectedness of one of the phases.

The statistical behavior of the spectrum is related to the extent that the eigenfunctions overlap. A key example is the Anderson theory of the metal-insulator transition (MIT) [1, 48], which provides a powerful theoretical framework for understanding when a disordered medium allows electronic transport, and when it does not. Indeed, for large enough disorder the electrons are localized in different places, with uncorrelated energy levels described by Poisson statistics [126, 88]. For small disorder, the wave functions are extended and overlap, giving rise to correlated Wigner-Dyson (WD) statistics [126, 88] with strong level repulsion [73]. In work on the effective complex permittivity for electromagnetic wave propagation through two phase composites in the long wavelength regime (or any other transport coefficient like thermal or electrical conductivity), we found an Anderson transition in spectral characteristics as the microstructure developed long range order in the approach to a percolation threshold [107]. We observe transitions in localization characteristics of the field vectors and associated transitions in spectral behavior from uncorrelated Poissonian statistics

to universal (repulsive) Wigner-Dyson statistics, connected to the Gaussian Orthogonal Ensemble (GOE) in random matrix theory. Mobility edges appear, analogous to Anderson localization where they mark the characteristic energies of the quantum MIT [73]. In [105] a novel class of two phase composites was introduced, based on Moiré patterns, that display exotic effective properties, and dramatic transitions in spectral behavior with very small changes in system parameters.

Over the past decade or so we have laid the groundwork for significant advances in the mathematical modeling of sea ice processes by developing Stieltjes integral representations for homogenized parameters in several new contexts of importance in the physics of sea ice and its role in climate. We focus on the central role that the spectral measure plays in determining effective behavior. The analytic continuation method is a powerful approach in homogenization that provides a robust mathematical framework for rigorously studying effective properties in the sea ice system. The body of work that is discussed here will advance our sea ice modeling capabilities and how sea ice is represented in global climate models, which will improve projections of the fate of sea ice and the ecosystems it supports. Moreover, the functions we study here in the sea ice context share the same mathematical properties as effective parameters in many other areas of science and engineering, so our work will advance knowledge of these other materials as well, as evidenced for example by [105], [70] and [75].

2 Percolation models.

Connectedness of one phase in a composite material is often the principal feature of the mixture geometry which determines effective behavior. For example, if highly conducting inclusions are sparsely distributed, forming a disconnected phase within a poorly conducting encompassing host, then the effective conductivity will be poor as well. However, if there are enough conducting inclusions so that they form connected pathways through the medium, then the effective conductivity will be much closer to that of the inclusions. Percolation theory [22, 127, 72, 24] focuses on connectedness in disordered and inhomogeneous media, and has provided the theoretical framework for describing the behavior of fluid flow through sea ice [65, 69, 62].

Consider the d -dimensional integer lattice \mathbb{Z}^d , and the square or cubic network of bonds joining nearest neighbor lattice sites. In the percolation model [22, 127, 72, 24], we assign to each bond a conductivity $\sigma_0 > 0$ with probability p , meaning it is open (black), and with probability $1 - p$ we assign $\sigma_0 = 0$, meaning it is closed. Two examples of lattice configurations are shown in Fig. 2. with $p = 1/3$ in (a) and $p = 2/3$ in (b). Groups of connected open bonds are called *open clusters*. In this model there is a critical probability p_c , $0 < p_c < 1$, the *percolation threshold*, at which the average cluster size diverges and an infinite cluster appears. For the $d = 2$ bond lattice $p_c = 1/2$. For $p < p_c$ the infinite cluster density $P_\infty(p) = 0$, while for $p > p_c$, $P_\infty(p) > 0$ and near the threshold, $P_\infty(p) \sim (p - p_c)^\beta$ as $p \rightarrow p_c^+$, where β is a universal critical exponent. It depends only on dimension and not on the details of the lattice. Let $x, y \in \mathbb{Z}^d$ and $\tau(x, y)$ be the probability that x and y belong to the same open cluster. Then for $p < p_c$, $\tau(x, y) \sim e^{-|x-y|/\xi(p)}$, and the correlation length $\xi(p) \sim (p_c - p)^{-\nu}$ diverges with a universal critical exponent ν as $p \rightarrow p_c^-$. as shown in Fig. 2 (c).

The effective conductivity $\sigma^*(p)$ of the lattice, now viewed as a random resistor (or conductor) network, defined via Kirchoff's laws, vanishes for $p < p_c$ like $P_\infty(p)$ since there are no infinite pathways. as shown in Fig. 2 (e). For $p > p_c$, $\sigma^*(p) > 0$, and near p_c , $\sigma^*(p) \sim \sigma_0(p - p_c)^t$, $p \rightarrow p_c^+$, where t is the conductivity critical exponent, with $1 \leq t \leq 2$ in $d = 2, 3$ [54, 58, 61], and numerical values $t \approx 1.3$ in $d = 2$ and $t \approx 2.0$ in $d = 3$ [127]. Consider a random pipe network with fluid permeability $k^*(p)$ exhibiting similar behavior $k^*(p) \sim k_0(p - p_c)^e$, where e is the permeability

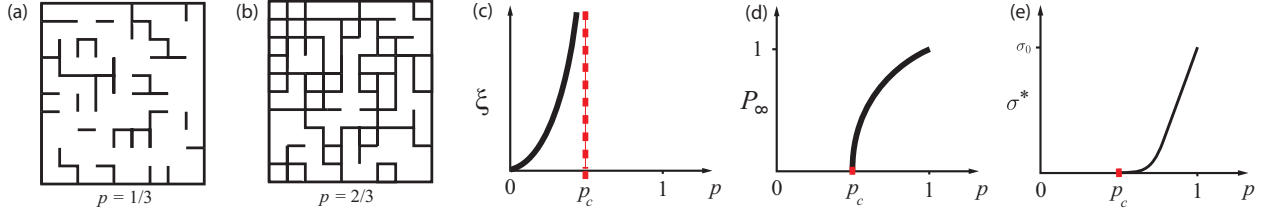


Figure 2: The two dimensional square lattice percolation model below its percolation threshold of $p_c = 1/2$ in (a) and above it in (b). (c) Divergence of the correlation length as p approaches p_c . The infinite cluster density of the percolation model is shown in (d), and the effective conductivity is shown in (e).

critical exponent, with $e = t$ [26, 123, 61]. Both t and e are believed to be universal – they depend only on dimension and not the lattice. Continuum models like the Swiss cheese model, can exhibit nonuniversal behavior with exponents different from the lattice case and $e \neq t$ [76, 52, 127, 122, 85].

3 Analytic continuation for two phase composites.

We now describe the *analytic continuation method* (ACM) for studying the effective properties of composites [12, 100, 56, 60]. This method has been used to obtain rigorous bounds on bulk transport coefficients of composite materials from partial knowledge of the microstructure, such as the volume fractions of the phases. Examples of transport coefficients to which this approach applies include the complex permittivity, electrical and thermal conductivity, diffusivity, magnetic permeability, and elasticity. In [55, 68, 67, 60, 63, 62, 66] rigorous bounds on the complex permittivity of sea ice were found.

To set ideas we focus on complex permittivity. Consider a two-phase random medium with local permittivity tensor $\epsilon(x, \omega)$, a spatially stationary random field in $x \in \mathbb{R}^d$ and $\omega \in \Omega$, where Ω is the set of realizations of the medium. We consider a two-phase locally isotropic medium, where the components ϵ_{jk} , $j, k = 1, \dots, d$, of ϵ satisfy

$$\epsilon_{jk}(x, \omega) = \epsilon(x, \omega) \delta_{jk}, \quad (1)$$

where d is dimension, δ_{jk} is the Kronecker delta and

$$\epsilon(x, \omega) = \epsilon_1 \chi_1(x, \omega) + \epsilon_2 \chi_2(x, \omega). \quad (2)$$

Later, we will consider a polycrystalline medium where ϵ is a non-trivial symmetric matrix. Here $\chi_i(x, \omega)$ is the characteristic function of medium $i = 1, 2$, equaling 1 for $\omega \in \Omega$ with medium i at x , and 0 otherwise, with $\chi_1 + \chi_2 = 1$. The random electric and displacement fields $E(x, \omega)$ and $D(x, \omega)$ satisfy

$$\nabla \times E = 0, \quad \nabla \cdot D = 0, \quad D = \epsilon E. \quad (3)$$

A variational problem establishes that E can be written as $E = E_f + E_0$ satisfying

$$E = E_f + E_0, \quad \nabla \times E_f = 0, \quad \langle D \cdot E_f \rangle = 0, \quad \langle E \rangle = E_0, \quad (4)$$

This basically amounts to saying curl-free and divergence-free fields are orthogonal (Helmholtz's theorem), but is rigorously established via the Lax-Milgram theorem [56].

The effective permittivity tensor ϵ^* is defined as $\langle D \rangle = \epsilon^* \langle E \rangle$, where $\langle \cdot \rangle$ is ensemble averaging over Ω or, by an ergodic theorem, spatial average over all of \mathbb{R}^d [56]. We prescribe that E_0 has direction e_k , the k th direction unit vector, and focus on the diagonal coefficient $\epsilon^* = \epsilon_{kk}^*$, with $\epsilon^* = \langle \epsilon E \cdot e_k \rangle$. The key step of the method is to obtain the following Stieltjes integral representation for ϵ^* [11, 100, 56, 102],

$$F(s) = 1 - \frac{\epsilon^*}{\epsilon_2} = \int_0^1 \frac{d\mu(\lambda)}{s - \lambda}, \quad s = \frac{1}{1 - \epsilon_1/\epsilon_2}, \quad (5)$$

where μ is a positive Stieltjes measure on $[0, 1]$. In the variable $h = \epsilon_1/\epsilon_2$, $F(s)$ is a *Stieltjes function* [59, 27, 112]. This formula arises from a resolvent formula for the electric field (in medium 1) [108],

$$\chi_1 E = s(sI - G)^{-1} \chi_1 e_k, \quad G = \chi_1 \Gamma \chi_1, \quad (6)$$

yielding $F(s) = \langle [(sI - G)^{-1} \chi_1 e_k] \cdot e_k \rangle$, where $\Gamma = -\nabla(-\Delta)^{-1} \nabla \cdot$ is a projection onto the range of the gradient operator ∇ and e_k is the standard basis vector in the k th direction. Formula (5) is the spectral representation of the resolvent and μ is the spectral measure of the self-adjoint operator $G = \chi_1 \Gamma \chi_1$ on $L^2(\Omega, P)$.

A critical feature of equation (5) is that the component parameters in s are separated from the geometrical information in μ . Information about the geometry enters through the moments

$$\mu_n = \int_0^1 \lambda^n d\mu(\lambda) = \langle G^n \chi_1 e_k \cdot \chi_1 e_k \rangle. \quad (7)$$

Then $\mu_0 = \phi$, where ϕ is the volume or area fraction of phase 1, such as the brine volume fraction, the open water area fraction or melt pond coverage and $\mu_1 = \phi(1-\phi)/d$ if the material is statistically isotropic. In general, μ_n depends on the $(n+1)$ -point correlation function of the medium. This integral representation yields rigorous *forward bounds* for the effective parameters of composites, given partial information on the microgeometry via the μ_n [12, 100, 56, 13]. One can also use the integral representations to obtain *inverse bounds*, allowing one to use data about the electromagnetic response of a sample, for example, to bound its structural parameters, such as the volume fraction of each of the components [98, 99, 32, 27, 148, 20, 31, 41, 70], see Section 5 for more details.

3.1 Spectral measure computations for two phase composites

Computing the spectral measure μ for a given 2D composite microstructure geometry first involves discretizing a two phase image of the composite into a square lattice filled with 1's and 0's corresponding to the two phases. On this square lattice the action of the differential operators ∇ and $\nabla \cdot$ are defined in terms of forward and backward difference operators [58]. Then the key operator $\chi_1 \Gamma \chi_1$, which depends on the geometry of the network via χ_1 , becomes a real-symmetric matrix M [108]. Here Γ is a (non-random) projection matrix which depends only on the lattice topology and boundary conditions, and χ_1 is a diagonal (random) projection matrix which determines the geometry and component connectivity of the composite medium [108].

The following theorem provides a rigorous mathematical formulation of integral representations for the effective parameters for finite lattice approximations of two component composite media. The electric field decomposition in this theorem is established in Theorem 4 of Appendix A below and the integral representation in equation (8) is established in Theorem 2.1 of [108].

Theorem 1. *For each $\omega \in \Omega$, let $M(\omega) = W(\omega) \Lambda(\omega) W(\omega)$ be the eigenvalue decomposition of the real-symmetric matrix $M(\omega) = \chi_1(\omega) \Gamma \chi_1(\omega)$. Here, the columns of the matrix $W(\omega)$ consist*

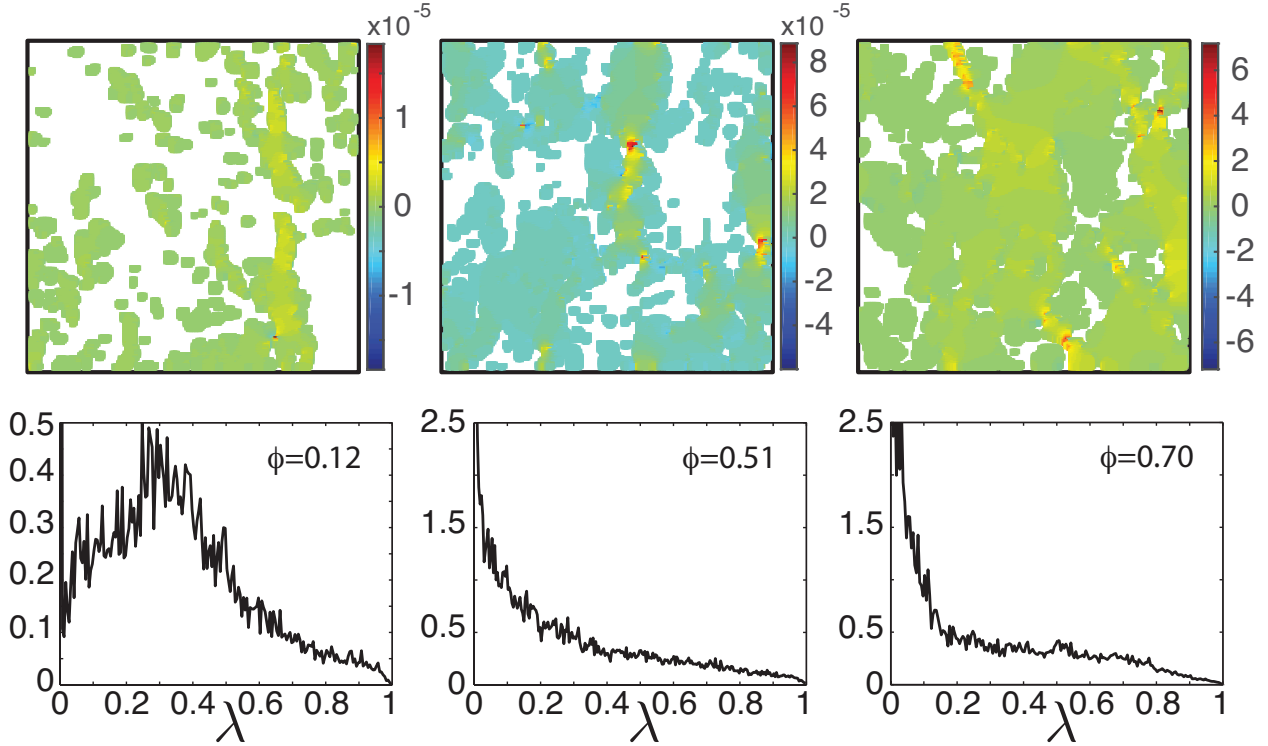


Figure 3: *Electric field and spectral function for sea ice brine microstructure.* Electric fields for X-ray CT images of 2D cross sections of 3D brine structures in sea ice (top) and corresponding spectral measures (bottom). As the brine fraction increases the fluid phase becomes increasingly connected and a delta function singularity in the spectral functions $\mu(\lambda)$ develops at $\lambda = 0$. This provides an electrical signature of brine connectivity, with a substantial increase in the strength of the electric field as the system attains global connectivity. Here, E_0 is taken to be vertically oriented.

of the orthonormal eigenvectors $w_i(\omega)$, $i = 1, \dots, N$, of $M(\omega)$ and the diagonal matrix $\Lambda(\omega) = \text{diag}(\lambda_1(\omega), \dots, \lambda_N(\omega))$ involves its eigenvalues $\lambda_i(\omega)$. Denote $Q_i = w_i w_i^T$ the projection matrix onto the eigen-space spanned by w_i and denote $\delta_{\lambda_i}(d\lambda)$ the Dirac δ -measure centered at λ_i . The electric field $E(\omega)$ satisfies $E(\omega) = E_0 + E_f(\omega)$, with $E_0 = \langle E(\omega) \rangle$ and $\Gamma E(\omega) = E_f(\omega)$, and the effective complex permittivity tensor ϵ^* has components ϵ_{jk}^* , $j, k = 1, \dots, d$, which satisfy

$$\epsilon_{jk}^* = \epsilon_2(\delta_{jk} - F_{jk}(s)), \quad F_{jk}(s) = \int_0^1 \frac{d\mu_{jk}(\lambda)}{s - \lambda}, \quad d\mu_{jk}(\lambda) = \sum_{i=1}^N \langle \delta_{\lambda_i}(d\lambda) \chi_1 Q_i \hat{e}_j \cdot \hat{e}_k \rangle. \quad (8)$$

From Theorem 1, the integral and $\chi_1 E$ in equations (5) and (6) have explicit representations in terms of the eigenvalues λ_i and eigenvectors u_i of M [108],

$$\chi_1 E = s \sum_i \frac{\sqrt{m_i}}{s - \lambda_i} u_i, \quad F(s) = \sum_i \left\langle \frac{m_i}{s - \lambda_i} \right\rangle, \quad m_i = |\chi_1 u_i \cdot \hat{e}_k|^2, \quad (9)$$

where \hat{e}_k plays the role of a standard basis vector on the lattice. To compute μ a non-standard generalization of the spectral theorem for matrices is required, due to the projective nature of the matrices χ_1 and Γ [108]. We developed a *projection method* that shows the spectral measure μ in (8) depends only on the eigenvalues and eigenvectors of random sub-matrices of Γ of size $N_1 \approx \phi N$

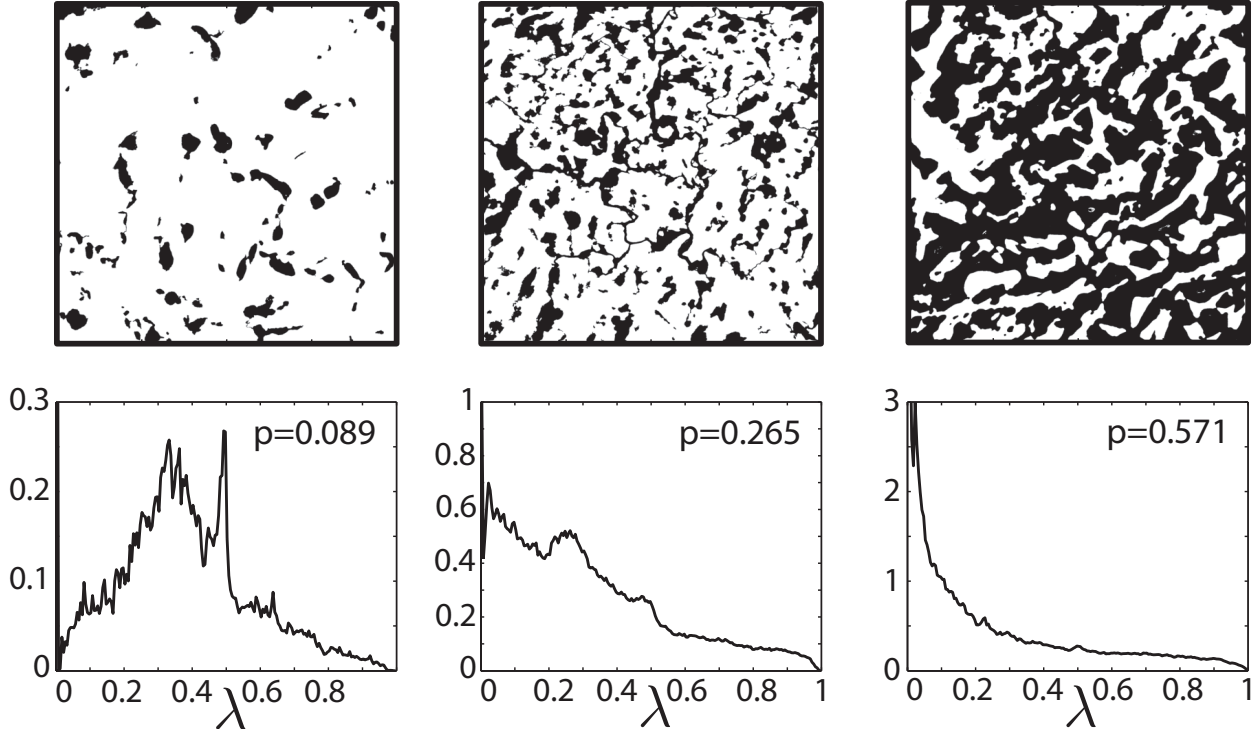


Figure 4: *Sea ice melt ponds*. Melt ponds on the surface of the sea ice (top) (images courtesy of Don Perovich) and corresponding spectral functions (bottom). As the melt pond area fraction increases the ice/water composites become increasingly connected and a delta function singularity in the spectral functions $\mu(\lambda)$ develops at $\lambda = 0$.

corresponding to diagonal components $[\chi_1]_{ii} = 1$, as the spectral weights m_i (Christoffel numbers) associated with eigenvectors satisfying $\chi_1 u_i = 0$ are themselves zero, $m_i = 0$ [108]. Fortunately, since these submatrices are much smaller for low volume fractions, this method greatly improves the efficiency and accuracy of numerical computations of μ .

The measure μ exhibits fascinating transitional behavior as a function of system connectivity. For example, in the case of a RRN with a low volume fraction p of open bonds, as shown in Fig. 2a, there are spectrum-free regions at the spectral endpoints $\lambda = 0, 1$ [112]. However, as p approaches the percolation threshold p_c [127, 136] and the system becomes increasingly connected, these spectral gaps shrink and then vanish [112, 82], leading to the formation of δ -components of μ at the spectral endpoints, *precisely* [112] when $p = p_c$ (and $p = 1 - p_c$ in $d = 3$). This leads to critical behavior of σ^* for insulating/conducting and conducting/superconducting systems [112]. This gap behavior of μ has led [59, 112] to a detailed description of these critical transitions in σ^* , which is analogous to the Lee–Yang–Ruelle–Baker description [6, 59] of the Ising model phase transition in the magnetization M . Moreover, using this gap behavior, all of the classical critical exponent scaling relations were recovered [112, 59] without heuristic scaling forms [46] but instead by using the *rigorous* integral representation for σ^* involving μ .

This spectral behavior emerges in all the systems mentioned above, such as the brine microstructure of sea ice [65, 69, 62] as shown in Fig. 3, melt ponds on the surface of Arctic sea ice [79] as shown in Fig. 4, and the sea ice pack itself [107]. This also gives rise to critical behavior of the electric field as shown in Fig. 3 for 2D cross sections of 3D brine microstructure, with E_0 taken to be in the vertical direction. Disconnected and weakly connected examples of brine microstructure have

small values of the electric field, while strongly connected brine microstructures are characterized by a substantial increase in the strength of the electric field. A similar behavior of the temperature gradient ∇T associated with the Stieltjes integral for the horizontal thermal conductivity of melt ponds atop Arctic sea ice is shown in Fig. 4.

3.2 Generalization to rank deficient setting

In the periodic setting, for example, the matrix Laplacian is singular so the matrix representation of $(-\Delta)^{-1}$ in Γ is not defined. We now extend the mathematical framework developed in [108] to this setting. To make the connection to the abstract Hilbert space [56] and full rank matrix [108] settings, we first give relevant details for these cases. Equation (6) for the abstract Hilbert space setting follows by applying the operator $-\nabla(-\Delta)^{-1}$ to the formula $\nabla \cdot D = 0$, yielding $\Gamma D = 0$. Equation (6) then follows by using $\Gamma E_f = E_f$ and $\Gamma E_0 = 0$ [108], since E_f is in the range of Γ and E_0 is constant [111, 110, 108]. The matrix form of $\nabla \cdot D = 0$ is $-\nabla^T D = 0$, where ∇ now represents the finite difference matrix representation of the gradient operator and $-\nabla^T$ is the finite difference representation of the divergence operator, with *negative* matrix Laplacian given by $\nabla^T \nabla$ [108]. As before, in [108] we applied the matrix $\nabla(\nabla^T \nabla)^{-1}$ to the formula $-\nabla^T D = 0$, yielding $\Gamma D = 0$, where $\Gamma = \nabla(\nabla^T \nabla)^{-1} \nabla^T$, and equation (6) follows the same way as before.

Now consider the singular value decomposition of the matrix gradient [111] of size $m \times n$, say, $\nabla = U \Sigma V^T$. Here U is a $m \times n$ matrix satisfying $U^T U = I_n$, Σ is a $n \times n$ diagonal matrix with diagonal entries consisting of the *singular values* of ∇ , and V is a $n \times n$ orthogonal matrix satisfying $V^T V = V V^T = I_n$, where I_n is the identity matrix of size n . When the matrix gradient is full rank it has n strictly positive singular values, so Σ is an invertible matrix and the matrix representation of Γ is given by $\Gamma = U U^T$. On the other hand, when the matrix gradient is singular we have $\Sigma = \text{diag}(\Sigma_1, 0, \dots, 0)$, where the diagonal matrix Σ_1 contains the n_1 strictly positive singular values of Σ and the rest of the singular values have value 0. Denoting U_1 and V_1 to be the columns of U and V corresponding to the diagonal entries of Σ_1 , we have $\nabla = U_1 \Sigma_1 V_1^T$, where Σ_1 is invertible and $U_1^T U_1 = V_1^T V_1 = I_{n_1}$. This enables us to write $-\nabla^T D = 0$ as $-V_1 \Sigma_1 U_1^T D = 0$, hence $U_1^T D = 0$ and $U_1 U_1^T D = 0$. Noting that the columns of U_1 span the range of the matrix gradient ∇ , the matrix $U_1 U_1^T$ is a projection onto the range of ∇ [111]. Defining $\Gamma = U_1 U_1^T$, equation (6) follows the same way as before. This clearly generalizes the full rank setting. More details are given in the appendix in Section A.

4 Analytic continuation for polycrystalline media

Sea ice is a composite material with polycrystalline microstructure on the millimeter to centimeter scale. When sea water freezes under turbulent forcing, granular sea ice forms, having small crystals with isotropic orientation angles. Columnar sea ice forms in quiescent conditions, with large crystals more strongly oriented in the vertical direction. Examples of granular and columnar sea ice polycrystal microgeometry are displayed in Fig. 5 (a) and (d).

Our analysis of the transport properties of random, uniaxial polycrystalline media [8] in [75] and a somewhat new formulation presented below shows the underlying, rigorous mathematical framework is a direct analogue of that for two-phase random media discussed in Sec. 3. For simplicity, we discuss electrical permittivity ϵ , keeping in mind the broader applicability to thermal conductivity κ , electric conductivity σ , etc. Polycrystalline materials, are composed of many crystallites (single crystals of varying size, shape, and orientation) that can have different local conductivities along different crystal axes. In contrast to equation (1), the local permittivity matrix of such media is

given by [102, 8]

$$\epsilon(x, \omega) = R^T \Phi R, \quad \Phi = \text{diag}(\epsilon_1, \dots, \epsilon_d), \quad (10)$$

where $R(x, \omega)$ is a random rotation matrix satisfying $R^T = R^{-1}$. For example, for $d = 2$ we have

$$\epsilon = R^T \begin{bmatrix} \epsilon_1 & 0 \\ 0 & \epsilon_2 \end{bmatrix} R, \quad R = \begin{bmatrix} \cos \theta & -\sin \theta \\ \sin \theta & \cos \theta \end{bmatrix}, \quad (11)$$

where $\theta = \theta(x, \omega)$ is the orientation angle, measured from the direction e_1 , of the polycrystallite which has an interior containing $x \in \mathbb{R}^d$ for $\omega \in \Omega$. In higher dimensions, $d \geq 3$, the rotation matrix R is a composition of “basic” rotation matrices R_i , e.g. $R = \prod_{j=1}^d R_j$, where the matrix $R_j(x, \omega)$ rotates vectors in \mathbb{R}^d by an angle $\theta_j = \theta_j(x, \omega)$ about the e_j axis. For example, in three dimensions

$$R_1 = \begin{bmatrix} 1 & 0 & 0 \\ 0 & \cos \theta_1 & -\sin \theta_1 \\ 0 & \sin \theta_1 & \cos \theta_1 \end{bmatrix}, \quad R_2 = \begin{bmatrix} \cos \theta_2 & 0 & \sin \theta_2 \\ 0 & 1 & 0 \\ -\sin \theta_2 & 0 & \cos \theta_2 \end{bmatrix}, \quad R_3 = \begin{bmatrix} \cos \theta_3 & -\sin \theta_3 & 0 \\ \sin \theta_3 & \cos \theta_3 & 0 \\ 0 & 0 & 1 \end{bmatrix}. \quad (12)$$

In the case of *uniaxial* polycrystalline media, the local permittivity along one of the crystal axes has the value ϵ_1 , while the permittivity along all the other crystal axes has the value ϵ_2 , so $\Phi = \text{diag}(\epsilon_1, \epsilon_2)$ for 2D (which is the general setting for 2D) and $\Phi = \text{diag}(\epsilon_1, \epsilon_2, \epsilon_2)$ for 3D. Equation (10) can be written in a more suggestive form in terms of the matrix $C = \text{diag}(1, 0, \dots, 0)$

$$\epsilon(x, \omega) = \epsilon_1 X_1(x, \omega) + \epsilon_2 X_2(x, \omega), \quad (13)$$

which is an analogue of equation (2). Here $X_1 = R^T C R$ and $X_2 = R^T (I - C) R$, where I is the identity matrix on \mathbb{R}^d . Since $R^T = R^{-1}$ and C is a diagonal projection matrix satisfying $C^2 = C$, it is clear that the X_i , $i = 1, 2$, are mutually orthogonal projection matrices satisfying

$$X_j^T = X_j, \quad X_j X_k = X_j \delta_{jk}, \quad X_1 + X_2 = I, \quad (14)$$

which are also properties of the characteristic functions χ_j in Sec. 3.

Equations (3) and (4) are also satisfied in this polycrystalline setting [56]. Similar to the derivation of equation (6) in Sec. 3, a resolvent representation for $X_1 E$ follows by applying the operator $-\nabla(-\Delta)^{-1}$ to the formula $\nabla \cdot D = 0$, yielding $\Gamma D = 0$. Then, using $\Gamma E_f = E_f$ and $\Gamma E_0 = 0$ [108] yields the following analogue of equation (6)

$$X_1 E = s(sI - G)^{-1} X_1 e_k, \quad G = X_1 \Gamma X_1, \quad (15)$$

yielding the integral representation in equation (5) for $F(s) = \langle [(sI - G)^{-1} X_1 e_k] \cdot e_k \rangle$. As in the two component setting, a critical feature of equation (5) is that the component parameters in s are separated from the geometrical information in μ . Information about the geometry enters through the moments in equation (7) with G given in (15) and χ_1 replaced by X_1 . The mass μ_0 of the measure μ_{jk} is given by

$$\mu_{jk}^0 = \langle X_1 e_j \cdot e_k \rangle, \quad \mu_{kk}^0 = \langle |X_1 e_k|^2 \rangle, \quad (16)$$

where the second equality follows from the fact that X_1 is a real-symmetric projection matrix. The statistical average $\langle |X_1 e_k|^2 \rangle$ in (16) can be thought of as the “mean orientation,” or as the

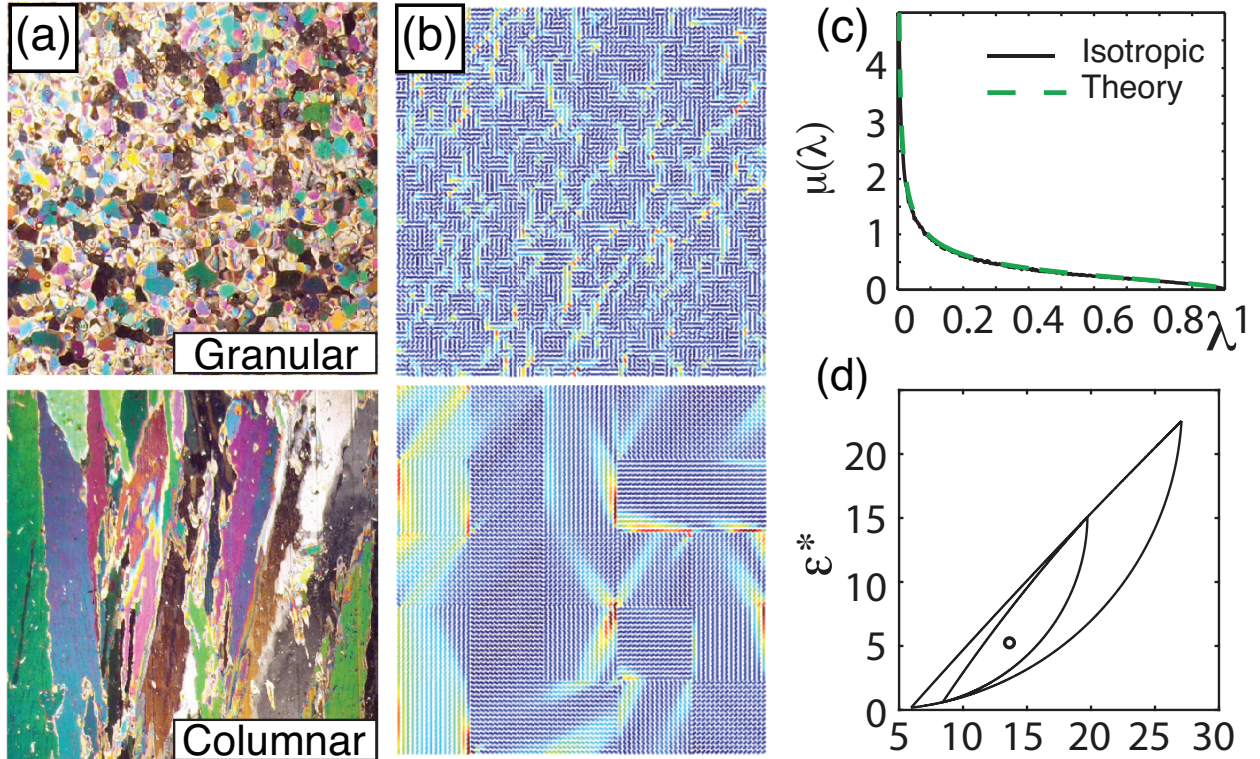


Figure 5: *Spectral analysis of polycrystalline media.* (a) Cross sections of polycrystalline microstructure for granular and columnar sea ice. (b) Discrete checkerboard polycrystal microstructure with isotropic crystallite orientations within the horizontal plane, with small (top) and large (bottom) crystallite size. Cool and warm colors correspond to low and high displacement fields. (c) The spectral function, a histogram representation of the spectral measure μ shown along with its theoretical prediction for such isotropic media [102]. (d) An example value of the complex effective permittivity of isotropic polycrystalline media captured by first and second order bounds [75].

percentage of crystallites oriented in the k^{th} direction. For example, in the case of two-dimensional polycrystalline media, $d = 2$, equation (11) implies that

$$\mu_{11}^0 = \langle \cos^2 \theta \rangle, \quad \mu_{22}^0 = \langle \sin^2 \theta \rangle, \quad \mu_{12}^0 = \langle \sin \theta \cos \theta \rangle. \quad (17)$$

Generalizing equation (12), with $R = \prod_{j=1}^d R_j$, to dimensions $d \geq 3$ shows that μ_{jk}^0 is a linear combination of averages of the form $\langle \prod_i \cos^{n_i} \theta_i \sin^{m_i} \theta_i \rangle$, where $n_i, m_i = 0, 1, 2, \dots$

The integral representation (5) for this polycrystalline setting yields rigorous *forward bounds* for the effective parameters of composites, given partial information on the microgeometry via the μ_n [75, 102], as shown in Fig. 5d below. One can also use the integral representations to obtain *inverse bounds*, allowing one to use data about the electromagnetic response of a sample, for example, to bound its structural parameters, such as the average crystallite orientation [75, 102], see Section ?? for more details.

4.1 Spectral measure computations for uniaxial polycrystalline materials

Computing the spectral measure μ for a given polycrystalline microgeometry first involves discretizing the composite into a square lattice with vertex values in the range $[0, 2\pi]$ corresponding to the

crystallite orientation angles at each vertex location. On this square lattice the action of the differential operators ∇ and $\nabla \cdot$ are defined in terms of forward and backward difference operators [58]. Then the key operator $X_1 \Gamma X_1$, which depends on the geometry of the network via X_1 , becomes a real-symmetric matrix M . Here Γ is as in Sec. 3.1 and X_1 is a banded (random) projection matrix which determines the geometry of the polycrystalline medium. In this setting, the integral and $X_1 E$ in equations (5) and (6) have explicit representations in terms of the eigenvalues λ_i and eigenvectors u_i of M [108] given by equation (9), and similarly the spectral measure is given by equation (8), with χ_1 replaced by X_1 .

The following theorem provides a rigorous mathematical formulation of integral representations for the effective parameters for finite lattice approximations of random uniaxial polycrystalline media.

Theorem 2. *For each $\omega \in \Omega$, let $M(\omega) = W(\omega)\Lambda(\omega)W(\omega)$ be the eigenvalue decomposition of the real-symmetric matrix $M(\omega) = X_1(\omega)\Gamma X_1(\omega)$. Here, the columns of the matrix $W(\omega)$ consist of the orthonormal eigenvectors $w_i(\omega)$, $i = 1, \dots, N$, of $M(\omega)$ and the diagonal matrix $\Lambda(\omega) = \text{diag}(\lambda_1(\omega), \dots, \lambda_N(\omega))$ involves its eigenvalues $\lambda_i(\omega)$. Denote $Q_i = w_i w_i^T$ the projection matrix onto the eigen-space spanned by w_i . The electric field $E(\omega)$ satisfies $E(\omega) = E_0 + E_f(\omega)$, with $E_0 = \langle E(\omega) \rangle$ and $\Gamma E(\omega) = E_f(\omega)$, and the effective complex permittivity tensor ϵ^* has components ϵ_{jk}^* , $j, k = 1, \dots, d$, which satisfy*

$$\epsilon_{jk}^* = \epsilon_2(\delta_{jk} - F_{jk}(s)), \quad F_{jk}(s) = \int_0^1 \frac{d\mu_{jk}(\lambda)}{s - \lambda}, \quad d\mu_{jk}(\lambda) = \sum_{i=1}^N \langle \delta_{\lambda_i}(d\lambda) X_1 Q_i \hat{e}_j \cdot \hat{e}_k \rangle. \quad (18)$$

We defer the proof of Theorem 2 to Section B, which holds for both of the settings where the matrix gradient is full rank or rank deficient. To numerically compute μ a non-standard generalization of the spectral theorem for matrices is required, due to the projective nature of the matrices X_1 and Γ [108]. In particular, in Section B we develop a *projection method* that shows the spectral measure μ in (18) depends only on the eigenvalues and eigenvectors of the upper left $N_1 \times N_1$ block of the matrix $R\Gamma R^T$, where $N_1 = N/d$. These submatrices are smaller by a factor of d , which improves the efficiency and numerical computations of μ by a factor of d^3 .

In Fig. 5 computations of the displacement field D are displayed for 2D polycrystalline media for small and large crystal sizes, along side cross sections of polycrystalline microstructure for granular and columnar sea ice. When the effective permittivity tensor ϵ^* is diagonal, such as the setting of isotropically oriented crystallites, the spectral measure for an infinite system is known in closed form [102] to be $d\mu(\lambda) = (\sqrt{(1-\lambda)/\lambda})(d\lambda/\pi)$, as shown in Fig. 5 (c). This measure has a singularity at $\lambda = 0$, which indicates that the material is electrically conductive, on macroscopic length scales [108, 112]. When the polycrystalline material has isotropic oriented crystallite angles, both the mass and first moment of the measure μ are known, which enables two nested bounds for ϵ to be computed [75], as shown in Fig. 5 (d).

5 Inverse homogenization: Inverse problem of recovery information about the structure of composites

Developed originally for the effective complex permittivity ϵ^* , the integral representation (5) yields rigorous *forward bounds* for the effective permittivity ϵ^* of two-component composites formed of materials with permittivity ϵ_1 and ϵ_2 , given partial information on the microgeometry via the moments μ_n [12, 100, 13, 56]. One can also use the integral representation to recover information

about the structure of composite material, this is the problem of **inverse homogenization**. For the inverse homogenization, it is important that the representation (5) separates information about the properties of the phases contained in the parameter s from information about the microgeometry contained in the measure μ and its moments $\mu_n = \langle G^n \chi_1 e_k \cdot \chi_1 e_k \rangle$ (7) via higher-order correlation functions of the geometry function χ_1 .

Spectral measure μ and its moments μ_n contain, in principle, all the geometrical information about the composite. For example, the mass μ_0 is the volume fraction ϕ of the first component in the composite,

$$\mu_0 = \int_0^1 d\mu(z) = \langle \chi_1 \rangle = \phi, \quad (19)$$

and the fraction of the second phase is $1 - \phi$. Connectivity information is also embedded in the spectral measure.

The basis for inverse homogenization is provided by the uniqueness theorem [27] which formulates the conditions under which the measure μ in the representation (5) can be uniquely reconstructed from measured data. For instance, electromagnetic data measured for a range of frequency of the applied electromagnetic field, are sufficient to uniquely recover the measure μ in (5). Such data are also sufficient for unique reconstruction of the moments μ_n [33], provided the permittivity of one of the phases is frequency dependent. Two major approaches to the inverse homogenization are the *reconstruction of the measure* μ [27, 33, 40, 148, 20, 21, 31, 41, 39, 70, 30] (and then calculating its moments) and *inverse bounds* for the structural parameters, such as, for example, the volume fraction of each of the components [98, 99, 34, 32, 27, 33], orientation of the crystals [75] or connectedness [115] of the structure.

When only a few data points are available, though the uniqueness theorem [27] is not immediately applicable, one can outline a set of measures consistent with the measurements,

$$\mathcal{M} = \{\mu : F_\mu(s) = 1 - \epsilon^*/\epsilon_2\}, \quad (20)$$

and determine an interval confining the first moment of the measure μ providing, for instance, an interval of uncertainty for the volume fraction of one material. For several data points corresponding to the same structure of the composite, such as for example, measurements at a few different frequencies, the bounds for the volume fraction are given by an intersection of all admissible intervals [34, 32, 137]. When the requirements for the measurements needed to uniquely reconstruct the spectral measure μ established by the uniqueness theorem are satisfied, the set \mathcal{M} is reduced to one point. But the map from the set of measures to the set of the microgeometries is not unique, and there is a variety of microstructures generating the same response under the applied field. Different microgeometries corresponding to the same sequence of moments μ_0, μ_1, \dots are the S -equivalent structures [27] that are not distinguishable by homogenized measurements.

An equivalent representation for function $F(s)$ in (5) using a logarithmic potential of the measure μ on the complex plane of variable s is [27]:

$$F(s) = \frac{\partial}{\partial s} \int \ln |s - z| d\mu(z), \quad \partial/\partial s = (\partial/\partial x - i \partial/\partial y), \quad s = \frac{1}{1 - \epsilon_1/\epsilon_2}. \quad (21)$$

The solution to the inverse problem of recovering the measure μ is constructed solving the minimization problem:

$$\min_\mu \|A\mu - F\|^2, \quad F(s) = 1 - \epsilon^*(s)/\epsilon_2 \quad (22)$$

where A is the integral operator in (21) or in (5), the norm is the L^2 -norm, $F = F(s)$, $s \in \mathbb{C}$, is the given function of the measured data, and \mathbb{C} is a curve on the complex plane corresponding

to the frequencies of the applied field. The solution of the minimization problem does not depend continuously on the data. Unboundedness of the operator A^{-1} leads to arbitrarily large variations in the solution, and the problem requires regularization to design a stable numerical algorithm [27]. Regularized inversion schemes and stable reconstruction algorithms to recover μ and its moments from data on the effective complex permittivity were developed in [27, 28, 33, 20, 31] based on L^2, TV , and non-negativity constraints, and constrained Pade approximation of the measure μ [148]. In application to imaging of bone structure, spectral measures μ computed with the regularization algorithms based on L^2 constrained minimization, from electromagnetic [20, 31, 70] and viscoelastic [19, 21, 31] data allow to distinguish the samples of healthy and osteoporotic bone via the different microstructures and the connectivity of the trabecular architecture.

With hydrostatic and deviatoric projections Λ_h and Λ_s onto the orthogonal subspaces of the second order tensors comprised of tensors proportional to the identity tensor and trace-free tensors, the Stieltjes integral representation was generalized in [31] to the effective viscoelastic modulus and to two-dimensional viscoelastic polycrystalline materials [29] under the assumption that the constituents have the same elastic bulk and different (elastic and viscoelastic) shear moduli. This representation was also used in inverse homogenization [19, 31, 30] for successful recovering the porosity of a composite from known viscoelastic shear modulus.

Other approaches to the volume fraction bounds include [47, 103, 133] based on estimates for higher order moments and on variational bounds, as well as direct inversion of known formulas or mixing rules [14, 89] for effective properties of composites with specific structure, however, an advantage of the methods discussed here, is their applicability without a priori assumption about the microgeometry.

Spectral coupling of various properties of composites. An important application of inverse homogenization is for indirect evaluating properties of materials through cross-coupling [102]. Different properties of composites are coupled through their microgeometry; this phenomenon has been known for a long time and used for estimating difficult to measure directly properties, from available data. The conventional approaches are based on empirical and semi-empirical relations, such as for instance, Kozeny-Carman or Katz-Tompson. These relations estimate permeability of a porous material characterizing the microstructure by a "formation factor" F which relates properties of one phase in the composite to the effective properties of the material.

In the *spectral coupling* method [27] based on properties of the Stieltjes representation (5), the spectral measure μ is associated with the geometric structural function as this is the function that couples various properties of the same material. The method of spectral coupling [27, 28, 35, 31] for two component composites based on this coupling of different properties of the composite through the spectral measure allows us to recover various transport properties of sea ice from the spectral measures computed using other measured properties. In particular, this approach results in an indirect method of calculation of the thermal conductivity [35] and hydraulic conductivity of polycrystalline sea ice, difficult to measure over large scales, from the effective complex permittivity data (recovered from radar measurements). The spectral coupling was extended to evaluating viscoelastic properties of two component composite in [31] in application to characterizing bone properties and microarchitecture.

Inverse homogenization for recovering microstructural parameters from effective property measurements is applicable to problems in remote sensing, medical imaging, non-destructive testing of materials, and allows for example, to use Synthetic Aperture Radar (SAR) remote sensing for assessing the structure and transport properties of sea ice.

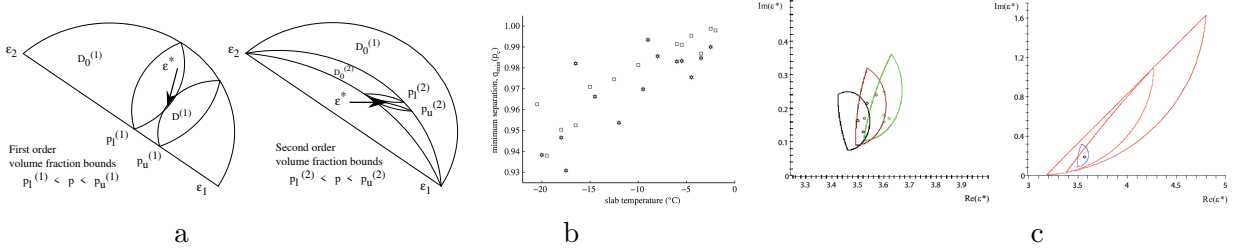


Figure 6: *Forward and Inverse bounds.* (a). Illustration of bounds on the volume fraction of one component in the mixture derived from first order anisotropic bounds (left panel), and from the second order isotropic bounds (right panel) for the effective permittivity [32]. The small lens shaped domains each contain ϵ^* of the anisotropic (left) and isotropic (right) composites corresponding to the volume fractions of the first component p_l and p_u which give the lower and upper bounds for the fraction of the first material. (b). Center figure shows lower bounds on separation parameter q_{min} versus temperature [115], calculated using data of the effective complex permittivity. The inverted data clearly indicate that as the ice warms, the separations of the brine inclusions decrease. Stars and squares indicate different sea ice slabs. (c). Polycrystalline bounds [75] for the permittivity sea ice (left) together with the measured effective permittivity of sea ice in [2]. Comparison of the polycrystalline bounds with the two-component bounds (right) shows a dramatic improvement over the classic two-component bounds as the new bounds include additional information about single crystal orientations. (Notice very different scales on the axes.)

5.1 Bounds for the moments of the spectral measure

The second approach to the inverse homogenization problem is calculating *inverse bounds* for the structural parameters, such as, for example, the volume fraction of each of the components [98, 99, 34, 32, 27], orientation of the crystals [75] or connectedness [115] of the structure. An analytical approach to estimating the volume fractions of materials in a composite [34, 32, 137] gives explicit analytic formulas for the first order inverse bounds on the volume fractions of the constituents in a general composite and second order inverse bounds on the fractions of the phases in an isotropic composite [32].

The inverse bounds are derived using analyticity of the effective complex permittivity of the composite. The first order bounds $p_l^{(1)}$ and $p_u^{(1)}$ for the volume fraction ϕ give the lower and upper bounds for the zero moment μ_0 of the measure μ or its mass in (19) [34, 32]:

$$p_l^{(1)} \leq \phi \leq p_u^{(1)}, \quad p_l^{(1)} = |f|^2 \frac{\text{Im}(\bar{s})}{\text{Im}(f)}, \quad p_u^{(1)} = 1 - \frac{|g|^2 \text{Im}(\bar{t})}{\text{Im}(g)}. \quad (23)$$

Here $t = 1 - s$, f is the known value of $F(s)$, and g is the known value of $G(t) = 1 - \epsilon^*/\epsilon_1$.

First and second order forward and inverse bounds are illustrated in Fig. 6(a) [32] where first order bounds for the effective complex permittivity of all anisotropic composites that could be formed from two materials of permittivity ϵ_1 and ϵ_2 are presented in the left panel, while the second order isotropic bounds are shown in right panel. The small lens shaped domains each contain the anisotropic (left) and isotropic (right) mixtures corresponding to the volume fractions ϕ of the first component equal to $p_l^{(q)}$ and $p_u^{(q)}$, $q = 1, 2$. The points $p_l^{(q)}$ and $p_u^{(q)}$ give the lower and upper bounds for the volume fraction of the first material in the composite. Superscripts $q = 1$ and $q = 2$ indicate the first and second order bounds.

For a set of data points $\epsilon^*(k)$, $k = 1, \dots, N$, corresponding to the same structure the bounds for the fraction ϕ of the first phase in the composite are given by an intersection of all admissible

intervals $p_l^{(q)}(k) \leq \phi \leq p_u^{(q)}(k)$:

$$P_l^{(q)} = \max_k p_l^{(q)}(k) \leq \phi \leq \min_k p_u^{(q)}(k) = P_u^{(q)}, \quad q = 1, 2. \quad (24)$$

Here $p_l^{(q)}(k)$ and $p_u^{(q)}(k)$ are, respectively, lower and upper bounds for the volume fraction ϕ calculated using the effective complex permittivity $\epsilon^*(k)$, and q is the order of the bounds, $q = 1$ for a general mixture, $q = 2$ for an isotropic composite.

In [32] this method was applied to estimating brine volume in sea ice from two data sets of 4.75 GHz measurements of the complex permittivity ϵ^* of sea ice [2] at -6°C and -11°C with fractions of brine $\phi = 0.036$ and $\phi = 0.0205$. Sea ice was considered as a composite of three components: pure ice, brine, and air; the effective complex permittivity of the mixture of ice and air was calculated with the Maxwell Garnett formula. The first order bounds estimate the brine volume fraction as $0.0213 \leq \phi \leq 0.0664$ and $0.0119 \leq \phi \leq 0.0320$, for the data set 1 and 2, respectively. The second order inverse bounds derived with the assumption of 2D isotropy in the horizontal plane give the following estimates for the brine volume fraction: $0.0333 \leq \phi \leq 0.0422$ for the first data set with brine volume $\phi = 0.036$, and $0.0189 \leq \phi \leq 0.0213$ for the second data set with volume fraction of brine $\phi = 0.0205$.

First order bounds are further extended to polycrystalline materials and allow to estimate the mean crystal orientation [75].

5.2 Matrix particle forward and inverse bounds

Another parameter important in characterizing the structure of composite material consisting of inclusions within a host matrix, is separation between the inclusions. Inclusion separation is an indicator of connectedness of phases – a key feature in critical behavior and phase transitions; the separation parameter may be used to estimate closeness to the percolation phase transition.

Composites with non-touching inclusions of one material embedded in a host matrix of different material are called matrix particle composites. For a matrix particle composite with separated inclusions tighter bounds on the effective complex permittivity may be obtained. In [115] sea-ice is considered as a matrix particle composite in which the brine phase contained in separated, circular discs of radii r_b randomly located on a horizontal plane, is surrounded by a “corona” of ice, with outer radius r_i . Such a material is called a q -material, where $q = r_b/r_i$. The minimal separation of brine inclusions is $2(r_i - r_b) = 2r_i(1 - q)$. In this case, as it is shown in [23], the support of μ in (5) lies in an interval $[s_m, s_M]$, $0 < s_m < s_M < 1$ such that $s_m = \frac{1}{2}(1 - q^2)$, $s_M = \frac{1}{2}(1 + q^2)$. The further the separation of the inclusions, the smaller the interval $[s_m, s_M]$, and the tighter the bounds. Smaller q values indicate well separated brine (and colder temperatures as in Fig. 6), and $q = 1$ corresponds to no restriction on the separation, with $s_m = 0$ and $s_M = 1$.

Two parameters characterizing the structure of the sea ice composite are volume fraction p of the brine inclusions and a separation parameter q that quantifies how close the inclusions are to each other. Using observed values of effective complex permittivity, and inverting the forward matrix particle bounds, information about these two parameters is obtained in [115] by solving exactly a reduced inverse spectral problem and bounding the volume fraction of the constituents, an inclusion separation parameter and the spectral gap of a self-adjoint operator that depends on the geometry of the composite. Inverse bounds for inclusion separation are shown in Fig. 6 [115], where the lower bound q_{min} is displayed versus temperature of the sea ice slab. The inverted data clearly indicate that as the ice warms, the separations of the brine inclusions decrease. It is remarkable that this important phenomenon is characterized from electromagnetic measurements through an inversion scheme.

5.3 Extension to polycrystalline composites

The method of inverse bounds [34, 32, 137] for structural parameters of a composite from measured effective properties was extended to polycrystalline materials in [75]. In the case of uniaxial polycrystalline composite, [75] develops bounds for the mean orientation of crystals in the sea ice from measured values of ice permittivity. As columnar and granular microstructures have different mean single crystal orientations [144] this inverse approach is useful for determining ice type when using remote sensing techniques.

The structures of different types of ice formed under different environmental conditions vary tremendously. For instance, for congelation ice frozen under calm conditions, the crystals are vertically elongated columns, and each crystal itself is a composite of pure ice platelets separating layers brine inclusions. The orientation of each crystal is determined by the direction that the c-axis points, which is perpendicular to the platelets. Finding the bounds for the crystals orientation we can electromagnetically distinguish columnar ice from granular ice. This is a critical problem in sea ice physics and biology, as these different structures have vastly different fluid flow properties (with 5% *vs.* 10% brine volume fraction at the percolation threshold) which affects melt pond evolution, nutrient replenishment, brine convection, and other mesoscale processes in the ice cover.

Bounds for the effective permittivity of polycrystalline composites are much tighter than those bounding the permittivity of a general two-component material and statistically isotropic two-component material for sea ice. Such polycrystalline bounds constructed in [75] are shown in two right panes of Fig. 6(c). Polycrystalline bounds for the permittivity sea ice (left) [75] (with the measured data on permittivity of sea ice [2]) provide a much tighter bound than general two-component material and statistically isotropic two-component material for sea ice given on the right (notice a different scale). This dramatic improvement over the classic two-component bounds is due to additional information about single crystal orientations included in the new bounds.

As was discussed in the polycrystal section, the zero moment μ_{kk}^0 in (16) of the measure μ in the integral representation of the effective properties of a uniaxial polycrystalline material is $\mu_{kk}^0 = \langle |X_1 e_k|^2 \rangle$. The statistical average $\langle |X_1 e_k|^2 \rangle$ can be viewed as the “mean crystal orientation” related to the percentage of crystallites oriented in the k^{th} direction.

Extending the inverse bounds method [34, 32, 137] to polycrystalline materials, the inverse polycrystalline bounds [75] estimate the mean crystal orientation by bounding the zero moment μ_{kk}^0 of the measure μ using measured data on the ice permittivity. This procedure gives an analytic estimate (the first order inverse bounds) for the range of values of the mean crystal orientation similar to (23):

$$\begin{aligned} \langle e_k^T X_1 e_k \rangle_l &\leq \langle e_k^T X_1 e_k \rangle \leq \langle e_k^T X_1 e_k \rangle_u, \\ \langle e_k^T X_1 e_k \rangle_l &= |f|^2 \frac{\text{Im}(\bar{s})}{\text{Im}(f)}, \quad \langle e_k^T X_1 e_k \rangle_u = 1 - |g|^2 \frac{\text{Im}(\bar{t})}{\text{Im}(g)}, \end{aligned} \quad (25)$$

Here X_1 is defined in the polycrystalline section as $X_1 = R^T C R$, f is the known value of $F(s)$ and g is the known value of $G(t) = 1 - \epsilon^*/\epsilon_1$ with $t = 1 - s$.

Inverse polycrystalline bounds computed in [75] for different types of sea ice, granular and columnar ice, show that the method allows revealing the type of ice based on electromagnetic data. For statistically isotropic granular ice shown in Fig. 5(a)-top, the inverse mean crystal orientation bounds [75] estimate the deviation angle as $\pi/2 \pm .02$ (with the true value $\pi/2$). The inverse mean crystal orientation bounds [75] for columnar ice (see Fig. 5(a)-bottom), estimate the angle of deviation of the crystal’s axis from the vertical as $20^\circ \pm 8^\circ$. These results demonstrate a significant difference in the reconstructed mean orientations of crystals in columnar and in granular ice and provide a foundation for distinguishing the types of ice using electromagnetic measurements.

Generalization of these polycrystalline bounds to the case when c -axis has a Gaussian distribution with known mean angle and the variance in the horizontal plane is developed in [97] as a method for obtaining bounds on effective permittivity of columnar sea ice that has a preferred direction in the horizontal plane due to a prevailing ocean current.

6 Analytic continuation for advection diffusion processes.

The enhancement of diffusive transport of passive scalars by complex fluid flow plays a key role in many important processes in the global climate system [142] and Earth’s ecosystems [44]. Advection of geophysical fluids intensifies the dispersion and large scale transport of heat [104], pollutants [38, 15, 125], and nutrients [44, 78] diffusing in their environment. In sea ice dynamics, where the ice cover couples the atmosphere to the polar oceans [142], the transport of sea ice can also be enhanced by eddy fluxes and large scale coherent structures in the ocean [143, 91, 45]. In sea ice thermodynamics, the temperature field of the atmosphere is coupled to the temperature field of the ocean through sea ice, a composite of pure ice with brine inclusions whose volume fraction and connectedness depend strongly on temperature [134, 69, 62]. Convective brine flow through the porous microstructure can enhance thermal transport through the sea ice layer [92, 146, 87].

Over the years a broad range of mathematical techniques have been developed that reduce the analysis of complex composite materials, with rapidly varying structures in space, to solving averaged, or *homogenized* equations that do not have rapidly varying data, and involve an effective parameter. Motivated by [116], the effective parameter problem was extended to complex velocity fields, with rapidly varying structures in both space and time, yielding the effective (eddy) viscosity and the effective (eddy) diffusivity tensors [96]. The effective parameter problem of (anomalous) super-diffusion and sub-diffusion is given in [17, 51]. Based on [96], Avellaneda and Majda [3, 4] adapted the ACM [56] to the advection diffusion equation and obtained a *Stieltjes integral representation* of the effective diffusivity tensor D^* , for flows with zero mean drift, involving the Péclet number ξ of the flow. This representation encapsulates the geometric complexity of the flow in a spectral measure associated with a random Hermitian operator (or matrix). Mimicking methods developed for composite media [102], they obtained rigorous bounds on the components of D^* . Moreover, in direct analogue of methods developed for composites [102], they also found velocity fields which realize these bounds, such as the famous confocal sphere configurations which realize the Hashin–Shtrikman bounds of composites [77, 4]. Remarkably, this method has also been extended to time dependent flows [5], flows with incompressible *nonzero* effective drift [117, 49], flows where particles diffuse according to linear collisions [118], and solute transport in porous media [16], which has a direct application to diffusive brine advection in sea ice. All yield Stieltjes integral representations of the symmetric and, when appropriate, the antisymmetric part of D^* .

We now briefly describe our recent results on this framework [87, 110, 111]. It is an important example of how Stieltjes integral representations can provide a rigorous basis for analysis of problems for sea ice involving advection diffusion processes. The dispersion of a cloud of passive scalars with density $\phi(t, x)$ diffusing with molecular diffusivity ϵ and being advected by a incompressible velocity field $u(t, x)$ satisfying $\nabla \cdot u = 0$ is described by the advection-diffusion equation

$$\frac{\partial \phi}{\partial t} = u \cdot \nabla \phi + \epsilon \Delta \phi, \quad \phi(0, x) = \phi_0(x). \quad (26)$$

Here, the initial density $\phi_0(x)$ and the fluid velocity field u are assumed to be given. In equation (26), the molecular diffusion constant $\epsilon > 0$, d is the spatial dimension of the system, ∂_t denotes partial differentiation with respect to time t , and $\Delta = \nabla \cdot \nabla = \nabla^2$ is the Laplacian. Moreover, $\psi \cdot \varphi = \psi^T \overline{\varphi}$,

ψ^T denotes transposition of the vector ψ , and $\bar{\varphi}$ denotes component-wise complex conjugation, with $\psi \cdot \psi = |\psi|^2$. Later, we will use this form of the dot product over complex fields, with built in complex conjugation. However, we emphasize that all quantities considered in this section are *real-valued*. The random paths of the tracer particles are determined [50] by the stochastic differential equation

$$dx(t) = u(t, x(t))dt + \sqrt{2\varepsilon} dW(t), \quad x(0) = x_0, \quad (27)$$

with the initial tracked tracer particle location x_0 given and $W(t)$ is standard Brownian motion (the Wiener process). Non-dimensionalizing and homogenizing (26) shows [96] that the effective behavior of thermal transport in sea ice is described by a diffusion equation involving an averaged scalar density $\bar{\phi}$ and a symmetric, constant [117] effective diffusivity tensor κ^* [132],

$$\frac{\partial \bar{T}(t, x)}{\partial t} = \nabla \cdot [\kappa^* \nabla \bar{T}(t, x)], \quad \bar{T}(0, x) = T_0(x). \quad (28)$$

For simplicity, we focus on a diagonal coefficient κ_{kk}^* , $k = 1, \dots, d$, of κ^* , set $\kappa^* = (\kappa^*)_{kk}$, and write $u = u_0 v$ involving the non-dimensional velocity field v . In these non-dimensional variables the Péclet number ξ and molecular diffusivity ε are related by $\xi = 1/\varepsilon$ [110].

Using a mathematical framework that is strikingly similar to that in Section 3, the effective diffusivity has the following Stieltjes integral representation [96, 4, 110, 111]

$$\kappa^* = \varepsilon(1 + \langle |\nabla w_k|^2 \rangle), \quad \langle |\nabla w_k|^2 \rangle = \int_{-\infty}^{\infty} \frac{d\nu(\lambda)}{\varepsilon^2 + \lambda^2}, \quad (29)$$

where $\langle \cdot \rangle$ denotes averaging over the space-time period cell for periodic flows [110, 111] or statistical average for random flows [3, 5]. An equivalent statement which emphasizes the connection to the two component composites setting in equation (5) is

$$F(\varepsilon) = 1 - \frac{\kappa^*}{\varepsilon} = \int_{-\infty}^{\infty} \frac{d\nu(\lambda)}{\varepsilon^2 + \lambda^2}. \quad (30)$$

Remarkably, the vector field $E(t, x) = \nabla w_k(t, x) + e_k$ satisfies equation (3) for two-component composite materials, with $D = \epsilon E$, $\epsilon = \varepsilon I + S$, $S = (-\Delta)^{-1} \partial_t + H$, and ϵ plays the role of the medium's electrical permittivity tensor [110, 111]. Here, $H(t, x)$ is the *stream matrix*, given in terms of the incompressible velocity field $v = \nabla \cdot H$ and satisfies $H^T = -H$ [4, 3]. When the flow is time-independent, $v = v(x)$, then $w_k = w_k(x)$ and $S = H(x)$. Moreover $\kappa^* = \epsilon^*$, with $\epsilon^* = (\epsilon^*)_{kk}$ defined above [110]. The integral representation for κ^* in Equation (29) follows from the resolvent formula

$$\nabla w_k = (\varepsilon I + i\Gamma S \Gamma)^{-1} g_k, \quad g_k = -\Gamma H e_k \quad (31)$$

which is an analogue of Equation (6). The *self-adjoint* operator $i\Gamma S \Gamma$, where $i = \sqrt{-1}$ is the imaginary unit, involves the same projection operator $\Gamma = -\nabla(-\Delta)^{-1}\nabla \cdot$ as the setting of two-component composites. Equation (29) shows that brine advection *enhances* the thermal diffusivity (and the thermal conductivity) of sea ice, since $\kappa^* \geq \varepsilon$.

Analytical calculations of the spectral measure ν are extremely difficult except for simple flows like shear flow [4]. However, Padé approximants $[L/M]$ provide rigorous, converging upper and lower bounds [7] for the *Stieltjes function* $f(z) = \langle |\nabla w_k|^2 \rangle / z = F/z$ in Equations (29) and (30), with $z = \varepsilon^{-2}$, using the moments ν_n of ν , $[M-1/M] \leq f(z) \leq [M/M]$, $f(z) = \sum_{n=0}^{\infty} (-1)^n \nu_{2n} z^n$. However, the lack of a method to calculate the moments ν_n of ν has impeded progress on obtaining

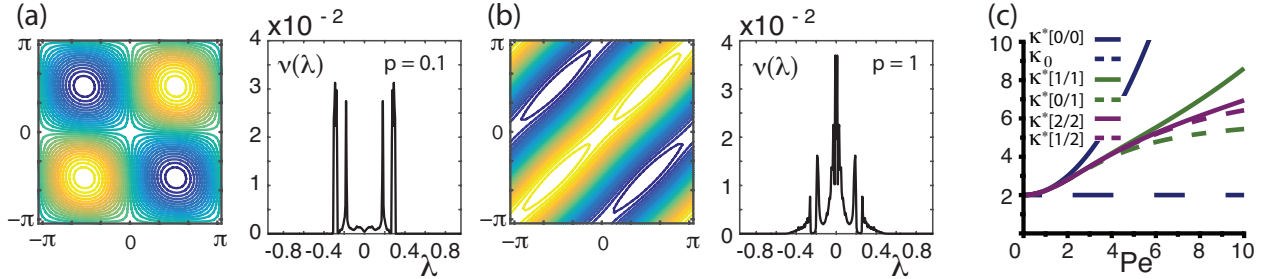


Figure 7: **Spectral behavior of homogenized diffusivities.** (a) Streamlines for BC-flow with velocity field $v = (C \cos y, B \cos x)$ and $B = C = 1$. (b) Padé approximant upper $\kappa^*[M/M]$ and lower $\kappa^*[M-1/M]$ bounds for κ^* , for various values of M , calculated for BC-flow with $C = B$, as a function of the flow strength B . (c) The spectral function (spectral masses m_j versus eigenvalues λ_j) computed via analogues of equations (9) and (18) [110].

explicit bounds for specific flows using this procedure [4, 3] since 1991! We have recently developed a mathematical framework [109] that can be used to compute, in principle, *all* of the moments ν_n associated with a spatially or space-time periodic brine velocity field v , hence Padé approximant bounds. Results for BC-flow, with $v = (C \cos y, B \cos x)$ and $B = C$ are shown in Figure 7(c).

6.1 Spectral measure computations for advection diffusion processes.

We have extended our numerical methods discussed for the two component media to compute the spectral measure ν for spatially periodic flows [110]. Computing the spectral measure μ for a given flow involves discretizing the spatially dependent stream matrix $H(x)$, which becomes a banded antisymmetric matrix satisfying $H^T = -H$. The projection matrix Γ is given by that in Section 3.1 and the key self-adjoint operator is given by $G = i\Gamma H \Gamma$, which becomes a *Hermitian* matrix. In this case, the integral in (29) and the resolvent in (31) are given in terms of the eigenvalues and eigenvectors of the matrix

$$\nabla w_k = \sum_i \frac{\sqrt{m_i}}{\varepsilon - \lambda_i} u_i, \quad \langle |\nabla w_k|^2 \rangle = \sum_i \left\langle \frac{m_i}{\varepsilon^2 + \lambda_i^2} \right\rangle, \quad m_i = |u_i \cdot g_i|^2, \quad (32)$$

which is analogous to equation (9). We have also developed Fourier methods for computing the spectral measure ν for space-time periodic flows [110].

These computations show that the origin in the space of the spectral parameter λ for advection diffusion plays the role of the spectral endpoints 0 and 1 for composite materials, with an increase in spectral mass giving rise to an advection-driven enhancement of effective diffusivity above the bare molecular diffusivity ε . For example, the closed streamlines of BC-cell-flow with fluid velocity field $v = (C \cos y, B \cos x)$ and $B = C = 1$ transport tracers in a short range periodic motion so long range transport is only possible due to molecular diffusion. Consequently, in the advection dominated regime with $\varepsilon \ll 1$ (or Péclet number $\xi \gg 1$) the effective diffusivity scales as $\kappa^* \sim \varepsilon^{1/2}$ [49, 50, 111], vanishing as $\varepsilon \rightarrow 0$. As shown in Fig. 7(a), this is reflected in the spectral measure ν by the lack of adequate mass near $\lambda = 0$ for the singular integrand $1/(\varepsilon^2 + \lambda^2)$ to overcome the multiplicative factor of ε for $\kappa^* = \varepsilon(1 + \langle |\nabla w_k|^2 \rangle)$ in (29).

On the other hand, when $B \neq C$ the streamlines elongate and connect to neighboring cells which gives rise to long range advection of tracers, even in the absence of molecular diffusion. This is reflected in the spectral measure by a buildup of adequate mass near $\lambda = 0$ for the singular

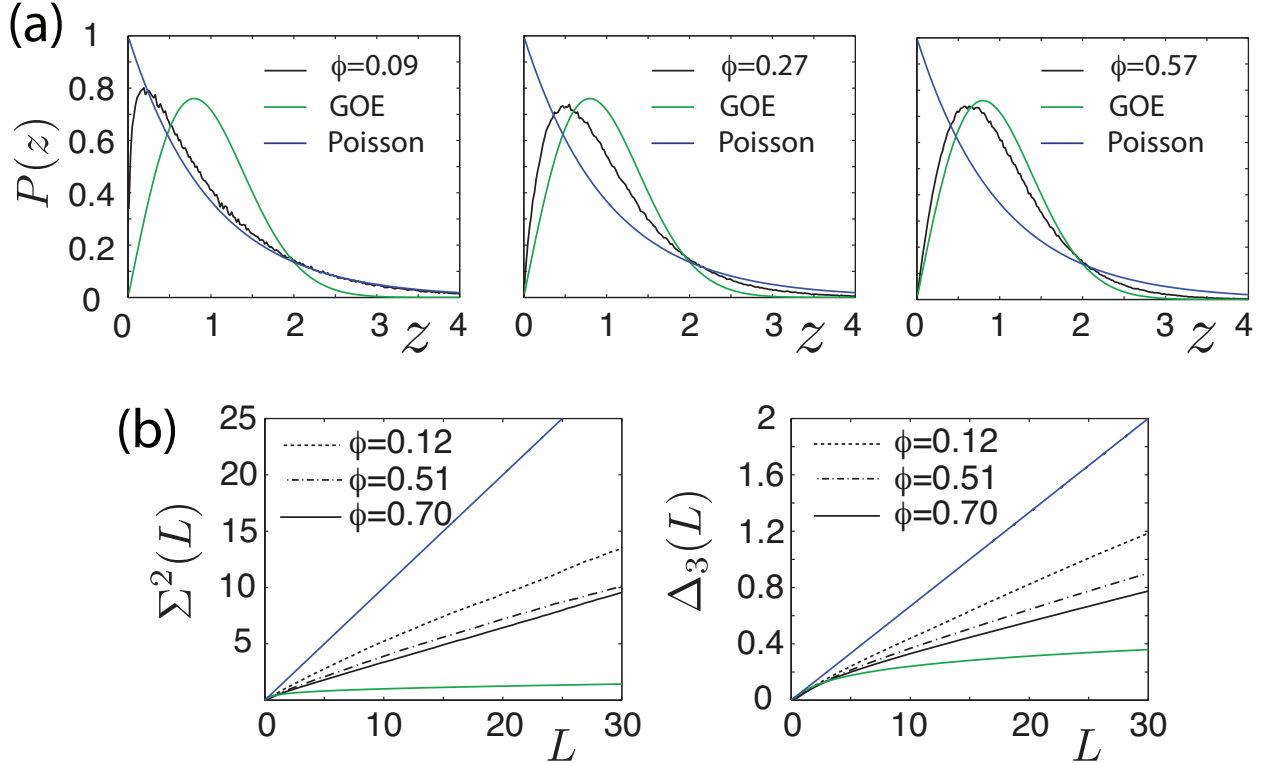


Figure 8: *Eigenvalue spacing statistics for the sea ice melt ponds (a) and long range eigenvalue statistics for brine structures in sea ice (b).* (a): Eigenvalue spacing distributions (ESD) $P(z)$ for melt ponds shown in Figure 4 corresponding to melt water area fractions 9%, 27%, and 57%. (b): Spectral statistics for brine structures shown in Figure 3 corresponding to area fractions of water 12%, 51%, and 70%. We see the transition to universal Wigner-Dyson statistics as ocean phases and brine phases become connected over the scale of the sample.

integrand $1/(\varepsilon^2 + \lambda^2)$ to overcome the multiplicative factor of ε for $\kappa^* = \varepsilon(1 + \langle |\nabla w_k|^2 \rangle)$ in (29), leading to a non-zero value of κ^* in the limit $\varepsilon \rightarrow 0$. This is a key example of how the behavior of the spectral measure ν governs the behavior of the bulk transport coefficient κ^* .

7 Random matrix theory for sea ice physics.

In random matrix theory (RMT) [73, 18, 42], long and short range correlations of the bulk eigenvalues away from the spectral edge [25, 73] for random matrices are measured using various eigenvalue statistics [73, 18], such as the eigenvalue spacing distribution (ESD) and the spectral rigidity Δ_3 and number variance Σ^2 . To observe statistical fluctuations of these bulk eigenvalues about the mean density, the eigenvalues must be unfolded [18, 73, 25, 120]. The localization properties of the eigenvectors are measured in terms of quantities such as the inverse participation ratio (IPR) [120, 48].

In [107], we found that as a percolation threshold is approached and long range order develops, the behavior of the ESD transitions from uncorrelated Poissonian toward obeying universal Wigner-Dyson (WD) statistics of the Gaussian Orthogonal Ensemble (GOE). The eigenvectors de-localize, and mobility edges appear [107], similar to the metal/insulator transition in solid state physics. We explored the transition in the 2D and 3D RRN, as well as in sea ice microstructures such as in

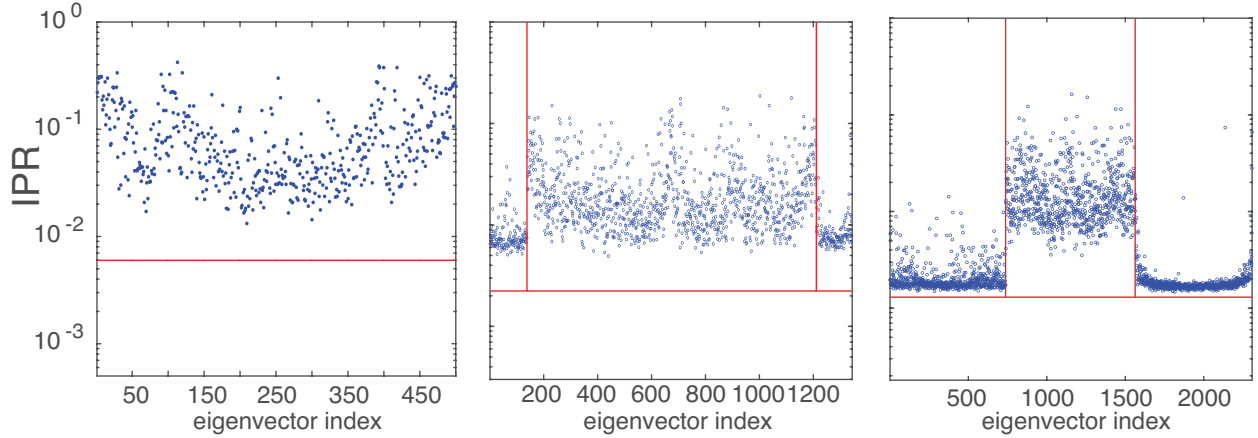


Figure 9: *Eigenvector localization for arctic melt pond microstructure.* The IPR’s of eigenvectors u_j associated with the melt pond microstructure shown above plotted versus eigenvalue index j and increasing connectedness from left to right. The vertical lines define the δ -components of μ while the horizontal lines mark the IPR value $I_{GOE} = 3/N_1$ for the Gaussian orthogonal ensemble (GOE) with matrix size $N_1 \approx \phi N$, where $N = L^d$.

2D discretizations of the brine microstructure of sea ice [65, 69, 62], melt ponds on Arctic sea ice [79], the sea ice pack itself, and porous human bone [70, 83, 20, 31].

For highly correlated WD spectra exhibited by, for example, real-symmetric matrices of the GOE, the nearest neighbor ESD $P(z)$ is accurately approximated by $P(z) \approx (\pi z/2) \exp(-\pi z^2/2)$, which illustrates *eigenvalue repulsion*, vanishing linearly as spacings $z \rightarrow 0$ [73, 128, 25]. In contrast, the ESD for uncorrelated Poisson spectra, $P(z) = \exp(-z)$, allows for significant level degeneracy [73]. In Fig.8(a) we display the ESDs for Poisson (blue) and WD (green) spectra, along with the behavior of the ESDs for the matrix $M = \chi_1 \Gamma \chi_1$, corresponding to the arctic sea ice melt ponds in Fig.4 with fluid area fraction ϕ . It shows that for sparsely connected systems, the behavior of the ESDs is well described by weakly correlated Poisson-like statistics [25]. With increasing connectedness, the ESDs transition toward highly correlated WD statistics with strong level repulsion. This behavior of the ESD reveals a mechanism for the collapse in the spectral gaps of μ . For sparsely connected systems, the weak level repulsion allows for significant level degeneracy and resonances in μ as shown in [108] for the 2D percolation model and in Fig.4 for arctic melt pond microstructure. As the system becomes increasingly connected, the level repulsion increases causing the eigenvalues to spread out which, in turn, causes the gaps in the measure near the spectral edges to collapse and subsequently form δ -components of the measure at the spectral endpoints $\lambda = 0, 1$. Our computations of Δ_3 and Σ^2 are shown in Fig.8(b) for the brine microstructure in Fig.3, with a transition toward that of the GOE, as the system becomes increasingly connected, indicating an increase in the long range correlations of the eigenvalues.

The eigenvectors u_j of $M = \chi_1 \Gamma \chi_1$, associated with the $N_1 \times N_1$ sub-matrices of Γ , also exhibit a connectedness driven transition in their localization properties. The IPR is defined as $I_j = \sum_i |u_j^i|^4$, $i, j = 1, \dots, N_1$, where u_j^i is the i th component of u_j . Eigenvectors of matrices in the GOE are known to be highly extended [42], with asymptotic value of the IPR given by $I_{GOE} = 3/N_1$ [120]. In [107], we found for the 2D and 3D percolation models that as p surpasses p_c and long range order is established in a RRN “**mobility edges**” form in the eigenvector IPR with a sudden increase in the number of extended eigenvectors, which is analogous to Anderson localization, where mobility edges mark the characteristic energies of the MIT [73]. Remarkably, the mobility edges for RRN are

due to very extended eigenstates associated with δ -components that form at the spectral endpoints *precisely* at the percolation threshold p_c (and $1 - p_c$ for 3D) [112], which control critical behavior in insulator/conductor and conductor/superconductor systems [112, 37, 14]. This phenomenon is shown for arctic melt pond microstructure in Fig. 9.

8 Conclusions

We have given a tour through various problems of sea ice physics concerned with homogenization and how they can be rigorously addressed with the powerful analytic continuation method and its extensions. The effective complex permittivity of sea ice treated as a two phase composite of pure ice with brine inclusions, or treated as a polycrystalline material, and the effective diffusivity for advection diffusion problems, are all Stieltjes functions of their variables. We showed how these functions have integral representations involving spectral measures which distill the mixture or velocity field geometries into the spectral properties of a self adjoint operator like the Hamiltonian in quantum physics. These spectral representations have been used to obtain rigorous forward and inverse bounds on effective transport coefficients for sea ice, and to develop a random matrix theory picture which uncovers parallels with Anderson localization and quantum transport in disordered media.

9 Acknowledgments

We gratefully acknowledge support from the Applied and Computational Analysis Program and the Arctic and Global Prediction Program at the US Office of Naval Research through grants N00014-18-1-2552, ONR Grant N00014-21-1-290, N00014-13-10291, N00014-15-1-2455, and N00014-18-1-2041. We are also grateful for support from the Division of Mathematical Sciences and the Division of Polar Programs at the US National Science Foundation (NSF) through Grants DMS-0940249, DMS-2136198, DMS-2111117, DMS-2206171, DMS-1715680, and DMS-1413454. Finally, we would like to thank the NSF Math Climate Research Network (MCRN), and especially Chris Jones, for supporting this work.

Appendix

A Existence of field decompositions

In this section, for the discrete setting in Sections 3.1 and 4.1, we prove that there exists an electric field E satisfying discrete versions of equations (3) and (4). Towards this goal, we follow [81] and consider the finite difference representations of the partial differential operators $\partial_i \rightarrow C_i, i = 1 \dots, d$, where d denotes dimension. The matrices C_i depend on boundary conditions which, without loss of generality, we take to be periodic boundary conditions. Denote the matrix representation of the gradient operator (using Matlab vertical block notation) by $\nabla = [C_1; \dots; C_d]$. The discretization of the divergence operator is given by $-\nabla^T$ and the discrete curl operator is given by [81]

$$C = \begin{bmatrix} O & -C_3 & C_2 \\ C_3 & O & -C_1 \\ -C_2 & C_1 & O \end{bmatrix} \text{ for 3D,} \quad (33)$$

$$C = [-C_2, C_1] \text{ for 2D.}$$

The operators C_i , $i = 1, 2, 3$, in (40) are normal and commute with each other [81],

$$C_i^T C_j = C_j C_i^T \text{ and } C_i C_j = C_j C_i, \text{ for } i, j = 1, 2, 3. \quad (34)$$

Consequently, the discrete form of equations (3) and (4), which we'll establish in this section, is

$$CE = 0, \quad -\nabla^T J = 0, \quad J = \epsilon E, \quad E = E_f + E_0, \quad CE_f = 0, \quad \langle J \cdot E_f \rangle = 0, \quad \langle E_f \rangle = 0, \quad (35)$$

where in this finite size discrete setting, $\langle \cdot \rangle$ denotes volume average followed by ensemble average [108, 111]. To set notation, denote by $\text{Ran}(B)$ and $\text{Ker}(B)$ the range and kernel (null space) of the matrix B , respectively [80]. Therefore, we seek to prove there exists a vector E satisfying $E \in \text{Ker}(C)$ such that $E = E_f + E_0$, where $E_f \in \text{Ker}(C)$ and $\langle E_f \rangle = 0$ so $\langle E \rangle = E_0$. Moreover, we seek to find a vector $J \in \text{Ker}(\nabla^T)$ satisfying $J = \epsilon E$ and $\langle J \cdot E_f \rangle = 0$.

We now summarize some useful identities relating the discrete representations of the gradient, divergence, and curl operators which follow from these properties of the matrices C_i [81],

$$\begin{aligned} \Delta &= \nabla \cdot \nabla \rightarrow -\nabla^T \nabla, \\ \mathbf{\Delta} &= \text{diag}(\Delta, \dots, \Delta) \rightarrow I_d \otimes (\nabla^T \nabla), \\ \nabla \times \nabla \times &\rightarrow C^T C, \\ \nabla \times \nabla \times &= \nabla(\nabla \cdot) - \mathbf{\Delta} \rightarrow -\nabla \nabla^T + I_d \otimes (\nabla^T \nabla), \\ \nabla \cdot (\nabla \times) &\rightarrow -\nabla^T C^T = 0, \\ \nabla \times \nabla &\rightarrow C \nabla = 0, \end{aligned} \quad (36)$$

where \otimes denotes the Kronecker product. The last two identities $\nabla^T C^T = 0$ and $C \nabla = 0$ in equation (36) indicate that

$$\text{Ran}(C^T) \subseteq \text{Ker}(\nabla^T), \quad \text{Ran}(\nabla) \subseteq \text{Ker}(C) \quad (37)$$

We can now restate our goal in (35) as, find "potentials" φ and ψ such that the vectors E and J in equation (35) satisfy $E = E_f + E_0$ with $E_f = \nabla \varphi$ and $E_0 \in \text{Ker}(\nabla)$, and $J = C^T \psi + J_0$, where $J_0 \in \text{Ker}(C^T)$. The last two identities (36) provide a relationship between rank and kernel of the operators C , ∇ , and their transposes. The fundamental theorem of linear algebra provides a relationship between the range of a matrix A and the kernel of its transpose A^T , which will be useful later in this section.

Theorem 3 (Fundamental theorem of linear algebra). *Let A be a real valued matrix of size $m \times n$ then*

$$\mathbb{R}^m = \text{Ran}(A) \oplus \text{Ker}(A^T), \quad \mathbb{R}^n = \text{Ran}(A^T) \oplus \text{Ker}(A), \quad (38)$$

where \oplus indicates $\text{Ran}(A)$ is orthogonal to $\text{Ker}(A^T)$, i.e., $\text{Ran}(A) \perp \text{Ker}(A^T)$, for example.

Applying Theorem 3 to the matrices ∇ and C^T indicates that $\mathbb{R}^m = \text{Ran}(\nabla) \oplus \text{Ker}(\nabla^T)$ and $\mathbb{R}^m = \text{Ran}(C^T) \oplus \text{Ker}(C)$. Therefore, from equation (37) we have that divergence-free fields are orthogonal to gradients (curl-free fields) and curl-free fields are orthogonal to $\text{Ran}(C^T)$ (divergence-free fields). This is a discrete version of the Helmholtz Theorem, which states that curl-free and divergence-free fields (or, in other words, the gradient and cycle spaces) are mutually orthogonal. This also establishes the important relationship

$$\text{Ran}(C^T) \perp \text{Ran}(\nabla). \quad (39)$$

Orthogonal bases can be given for each of the mutually orthogonal spaces in equation (38) through the singular value decomposition (SVD) [80] of the matrix $A = U\Sigma V^T$, which also provides important information relating the matrices C , ∇ , etc. Here U and V are orthogonal matrices of size $m \times m$ and $n \times n$ satisfying $U^T U = U U^T = I_m$ and $V^T V = V V^T = I_n$, where I_m is the identity matrix of size m . Moreover, Σ is a diagonal matrix of size $m \times n$ with diagonal components consisting of the positive *singular values* ν_i , $i = 1, \dots, n$, of the matrix A satisfying $\nu_1 \geq \nu_2 \geq \dots \geq \nu_\rho > 0$ and $\nu_{\rho+1} = \nu_{\rho+2} = \dots = \nu_n = 0$, where ρ is the rank of A . Writing the matrix Σ in block form we have

$$\Sigma = \begin{bmatrix} \Sigma_1 & O_1 \\ O_1^T & O_2 \\ O_3 & O_4 \end{bmatrix}, \quad (40)$$

where Σ_1 is a diagonal matrix of size $\rho \times \rho$ with diagonal consisting of the strictly positive singular values, O_1 and O_2 , are matrices of zeros of size $\rho \times (n - \rho)$ and $(n - \rho) \times (n - \rho)$, and the bottom block of zeros $[O_3, O_4]$ is of size $(m - n) \times n$. Write the matrices U and V in block form as $U = [U_1, U_0, U_2]$ and $V = [V_1, V_0]$, where U_1 and V_1 are the columns of U and V corresponding to the strictly positive singular values in Σ_1 , U_0 and V_0 correspond to the the singular values with value zero, $\nu_i = 0$, and U_2 corresponds to the bottom block of zeros $[O_3, O_4]$ in Σ . Taking in account all the blocks of zeros in Σ , we can write $A = U_1 \Sigma_1 V_1^T$. We now state a well known fact about the SVD of the matrix A [80].

$$\text{Range}(A) = \text{Col}(U_1), \quad \text{Ker}(A) = \text{Col}(V_0), \quad \text{Range}(A^T) = \text{Col}(V_1), \quad \text{Ker}(A^T) = \text{Col}([U_0, U_2]), \quad (41)$$

where $\text{Col}(B)$ denotes the column space of the matrix B , i.e., the space spanned by the columns of B .

Applying the SVD to the matrices $\nabla = U^\times \Sigma^\times [V^\times]^T$ and $C^T = U^\bullet \Sigma^\bullet [V^\bullet]^T$ and using the orthogonality of the columns of the matrices U_1 and V_1 and the invertability of Σ_1 , from $C\nabla = 0$ in (36) we have $[U^\bullet]^T U^\times = 0$, and similarly $\nabla^T C^T = 0$ implies $[U^\times]^T U^\bullet = 0$. The formula $[U^\bullet]^T U^\times = 0$ is a restatement of equation (39). Writing $U^\times = [U_1^\times, U_0^\times, U_2^\times]$ and $U^\bullet = [U_1^\bullet, U_0^\bullet, U_2^\bullet]$ we have established the $\text{Ran}(\nabla) = \text{Col}(U_1^\times)$, $\text{Ran}(C^T) \subseteq \text{Ker}(\nabla^T) = \text{Col}([U_0^\times, U_2^\times])$. Also, since $\text{Ran}(C^T) = \text{Col}(U_1^\bullet)$ and $\text{Ran}(C^T) \perp \text{Ran}(\nabla)$, we can write

$$U^\times = [U_1^\times, U_0^{\times\bullet}, U_1^\bullet], \quad U^\bullet = [U_1^\bullet, U_0^{\times\bullet}, U_1^\times], \quad (42)$$

where the columns of $U_0^{\times\bullet}$ are orthogonal to both the $\text{Ran}(C^T)$ and the $\text{Ran}(\nabla)$. Since $U^\times [U^\times]^T = I_m$ we have the *resolution of the identity*

$$\Gamma_\times + \Gamma_0 + \Gamma_\bullet = I_m, \quad \Gamma_\times = U_1^\times [U_1^\times]^T, \quad \Gamma_\bullet = U_1^\bullet [U_1^\bullet]^T, \quad \Gamma_0 = U_0^{\times\bullet} [U_0^{\times\bullet}]^T, \quad (43)$$

where Γ_\times , Γ_\bullet , and Γ_0 , are mutually orthogonal projection matrices onto $\text{Ran}(\nabla)$, $\text{Ran}(C^T)$ and the orthogonal complement of $\text{Ran}(\nabla) \cup \text{Ran}(C^T)$. We are now ready to state the main result of this section as the following theorem.

Theorem 4. *Let the electric and current fields E and J satisfy*

$$CE = 0, \quad -\nabla^T J = 0, \quad J = \epsilon E. \quad (44)$$

Then, there exists a "potential" φ and vector E_0 such that $E = E_f + E_0$, where $E_f = \nabla\varphi$, $I_d \otimes (\nabla^T \nabla) E_0 = 0$, $CE_f = 0$, $\langle J \cdot E_f \rangle = 0$, and $\langle E_f \rangle = 0$.

Proof. From the resolution of the identity in equation (43) we have $E = (\Gamma_{\times} + \Gamma_0 + \Gamma_{\bullet})E$. Since Γ_{\bullet} projects onto the $\text{Ran}(C^T)$, $\mathbb{R}^m = \text{Ran}(C^T) \oplus \text{Ker}(C)$, and $E \in \text{Ker}(C)$ we have $\Gamma_{\bullet}E = 0$. Denoting by $E_f = \Gamma_{\times}E$, since $U_1^{\times} = \nabla V_1^{\times} [\Sigma_1^{\times}]^{-1}$, we can write $E_f = \nabla \varphi$, where $\varphi = V_1^{\times} [\Sigma_1^{\times}]^{-1} [U_1^{\times}]^T E$. Denote $E_0 = \Gamma_0 E$. Since $\Gamma_{\times} E_0 = 0$, Γ_{\times} is a projection onto $\text{Ran}(\nabla)$, and $\mathbb{R}^m = \text{Ran}(\nabla) \oplus \text{Ker}(\nabla^T)$, we have $E_0 \in \text{Ker}(\nabla^T)$. Similarly, since $\Gamma_{\bullet} E_0 = 0$, Γ_{\bullet} is a projection onto $\text{Ran}(C^T)$, and $\mathbb{R}^m = \text{Ran}(C^T) \oplus \text{Ker}(C)$, we have $E_0 \in \text{Ker}(C)$. Since $E_0 \in \text{Ker}(C) \cap \text{Ker}(\nabla^T)$ we have from (36) that

$$0 = C^T C E_0 = (-\nabla \nabla^T + I_d \otimes (\nabla^T \nabla)) E_0 = I_d \otimes (\nabla^T \nabla) E_0. \quad (45)$$

From $\text{Ran}(\nabla) \subseteq \text{Ker}(C)$ in equation (37) and $E_f = \nabla \varphi$ we have $C E_f = C \nabla \varphi = 0$. We also have from $\nabla^T J = 0$ that $J \cdot E_f = J \cdot \nabla \varphi = \nabla^T J \cdot \varphi = 0$. Finally, the volume average of $\nabla \varphi$ is a telescoping sum, so $\langle E_f \rangle = 0$. This concludes our proof of the theorem. \square

Corollary 1. *Let the electric and current fields E and J satisfy*

$$C E = 0, \quad -\nabla^T J = 0, \quad J = \sigma E. \quad (46)$$

Then, there exists a "potential" ψ and vector J_0 such that $J = J_f + J_0$, where $J_f = C^T \psi$, $I_d \otimes (\nabla^T \nabla) J_0 = 0$, $\nabla^T J_f = 0$, $\langle J_f \cdot E \rangle = 0$, and $\langle J_f \rangle = 0$.

Proof. From the resolution of the identity in equation (43) we have $J = (\Gamma_{\times} + \Gamma_0 + \Gamma_{\bullet})J$. Since Γ_{\times} projects onto the $\text{Ran}(\nabla)$, $\mathbb{R}^m = \text{Ran}(\nabla) \oplus \text{Ker}(\nabla^T)$, and $J \in \text{Ker} \nabla^T$ we have $\Gamma_{\times} J = 0$. Denoting by $J_f = \Gamma_{\bullet} J$, since $U_1^{\bullet} = C^T V_1^{\bullet} [\Sigma_1^{\bullet}]^{-1}$, we can write $J_f = C^T \psi$, where $\psi = V_1^{\bullet} [\Sigma_1^{\bullet}]^{-1} [U_1^{\bullet}]^T J$. Denote $J_0 = \Gamma_0 J$. Exactly the same as in the proof of Theorem 4, we have $J_0 = I_d \otimes (\nabla^T \nabla) J_0$. From $\text{Ran}(C^T) \subseteq \text{Ker}(\nabla^T)$ in equation (37) and $J_f = C^T \psi$ we have $\nabla^T J_f = \nabla^T C^T \psi = 0$. Exactly the same as in the proof of Theorem 4, we also have $J_f \cdot E = 0$ and $\langle J_f \rangle = 0$. This concludes our proof of the theorem. \square

We end this section by noting that in the full rank setting, where Σ has all strictly positive singular values, so $\Sigma_1 = \Sigma$, then

$$\Gamma_{\times} = \nabla (\nabla^T \nabla)^{-1} \nabla^T, \quad \Gamma_{\bullet} = C^T (C C^T)^{-1} C.$$

The original formulations of this mathematical framework was given in terms of these projection matrices, or continuum generalizations [56, 108]. The formulation given in this section generalizes the discrete setting to cases where the matrix gradient is rank deficient, such as the case of periodic boundary conditions. This is necessary

B Proof of Theorem 2

In this section we provide the proof for Theorem 2 and a projection method for a numerically efficient projection method for computation of spectral measures and effective parameters for uniaxial polycrystalline media. We will use the results from Section A but for notational simplicity we will use Γ instead of Γ_{\times} . Corollary 2 below follows immediately from the proof of Theorem 2 and the results of Section A, which provides an integral representation for the effective resistivity ρ^* involving the matrix $X_2 \Gamma_{\bullet} X_2$ and is analogous to the representation of ρ^* for the two-component composite setting in [108].

From the close analogues of this polycrystalline setting with the two-component setting discussed in Sec. 3, the proof of this theorem is analogous to Theorem 2.1 in [108]. To shorten the theorem proof here, we will refer to [108] for some of the technical details. From Section A and the paragraph

in [108] containing equations 2.39 and 2.40, with χ_1 replaced by X_1 , we just need to prove that the functional $F_{jk}(s) = \langle (sI - X_1\Gamma X_1)^{-1} X_1 \hat{e}_j \cdot \hat{e}_k \rangle$ has the integral representation displayed in equation (18). In the process, we will also establish a projection method for the numerically efficient, rigorous computation of μ_{jk} . This projection method is summarized by equations (55)–(57) below.

In equation (14) we defined the real-symmetric mutually orthogonal projection matrices X_i , $i = 1, 2$, in terms of the *spatially dependent* rotation matrix R and $C = \text{diag}(1, 0, \dots, 0)$, all matrices of size $d \times d$. The paragraph in [108] containing equations 2.28–2.30 describes how to bijectively map these $d \times d$ matrices to $N \times N$ matrices that are *not* spatially dependent, where $N = L^d$. Under this mapping, R becomes a banded rotation matrix satisfying $R^T = R^{-1}$ and C becomes $C = \text{diag}(I_1, 0_1, \dots, 0_1)$, where I_1 and 0_1 are the identity and null matrices of size $N_1 = L^d$, and the vector e_1 is mapped to $\hat{e}_1 = (1, 1, \dots, 1, 0, 0, \dots, 0)$, with L^d ones in the first components and zeros in the rest of the components. Writing $X_1\Gamma X_1 = R^T(CR\Gamma R^T C)R$ we have

$$\begin{aligned} X_1\Gamma X_1 &= R^T \begin{bmatrix} \Gamma_1 & 0_{12} \\ 0_{21} & 0_{22} \end{bmatrix} R = R^T \begin{bmatrix} W_1\Lambda_1 W_1^T & 0_{12} \\ 0_{21} & 0_{22} \end{bmatrix} R \\ &= R^T \begin{bmatrix} W_1 & 0_{12} \\ 0_{21} & I_2 \end{bmatrix} \begin{bmatrix} \Lambda_1 & 0_{12} \\ 0_{21} & 0_{22} \end{bmatrix} \begin{bmatrix} W_1^T & 0_{12} \\ 0_{21} & I_2 \end{bmatrix} R, \end{aligned} \quad (47)$$

where I_2 is the identity matrix of size $N_2 \times N_2$, with $N_2 = N - N_1 = L^d(d - 1)$, and 0_{ab} denotes a matrix of zeros of size $N_a \times N_b$, $a, b = 1, 2$. Moreover, Γ_1 is the $N_1 \times N_1$ upper left principal submatrix of $R\Gamma R^T$ and $\Gamma_1 = W_1\Lambda_1 W_1^T$ is its eigenvalue decomposition. As Γ_1 is a real-symmetric matrix, W_1 is an orthogonal matrix [80]. Also, since $R\Gamma R^T$ is a similarity transformation of a projection matrix and C is a projection matrix, Λ_1 is a diagonal matrix with entries $\lambda_i^1 \in [0, 1]$, $i = 1, \dots, N_1$, along its diagonal [80, 43].

Consequently, equation (47) implies that the eigenvalue decomposition of the matrix $X_1\Gamma X_1$ is given by

$$X_1\Gamma X_1 = W\Lambda W^T, \quad W = R^T \begin{bmatrix} W_1 & 0_{12} \\ 0_{21} & I_2 \end{bmatrix}, \quad \Lambda = \begin{bmatrix} \Lambda_1 & 0_{12} \\ 0_{21} & 0_{22} \end{bmatrix}. \quad (48)$$

Here, W is an orthogonal matrix satisfying $W^T W = W W^T = I$, I is the identity matrix on \mathbb{R}^N , and Λ is a diagonal matrix with entries $\lambda_i \in [0, 1]$, $i = 1, \dots, N$, along its diagonal.

The eigenvalue decomposition of the matrix $X_1\Gamma X_1$ in equation (48) demonstrates that its resolvent $(sI - X_1\Gamma X_1)^{-1}$ is well defined for all $s \in \mathbb{C} \setminus [0, 1]$. In particular, by the orthogonality of the matrix W , it has the following useful representation $(sI - X_1\Gamma X_1)^{-1} = W(sI - \Lambda)^{-1} W^T$, where $(sI - \Lambda)^{-1}$ is a diagonal matrix with entries $1/(s - \lambda_i)$ along its diagonal. This, in turn, implies that the functional $F_{jk}(s) = \langle (sI - X_1\Gamma X_1)^{-1} X_1 \hat{e}_j \cdot \hat{e}_k \rangle$ can be written as

$$F_{jk}(s) = \langle (sI - \Lambda)^{-1} [X_1 W]^T \hat{e}_j \cdot W^T \hat{e}_k \rangle. \quad (49)$$

Since $R^T = R^{-1}$ and $X_1 = R^T C R$, equation (48) implies that

$$X_1 W = R^T \begin{bmatrix} W_1 & 0_{12} \\ 0_{21} & 0_{22} \end{bmatrix} \implies X_1 w_i = \begin{cases} w_i, & \text{for } i = 1, \dots, N_1, \\ 0, & \text{otherwise.} \end{cases} \quad (50)$$

This and the formula for W in (48) imply that

$$[X_1 W]^T \hat{e}_j \cdot W^T \hat{e}_k = [X_1 W]^T \hat{e}_j \cdot [X_1 W]^T \hat{e}_k. \quad (51)$$

We are ready to provide the integral representation displayed in (18) for the functional $F_{jk}(s)$ in equation (49). Denote by $Q_i = w_i w_i^T$, $i = 1, \dots, N$, the symmetric, mutually orthogonal projection matrices, $Q_\ell Q_m = Q_\ell \delta_{\ell m}$, onto the eigen-spaces spanned by the orthonormal eigenvectors w_i . Equation (50) implies that $X_1 Q_i = Q_i X_1 = X_1 Q_i X_1$, as $X_1 Q_i = Q_i$ for $i = 1, \dots, N_1$, $X_1 Q_i = 0$ otherwise, and X_1 is a symmetric matrix. These properties allow us to write the quadratic form $[X_1 W]^T \hat{e}_j \cdot [X_1 W]^T \hat{e}_k$ as

$$[X_1 W]^T \hat{e}_j \cdot [X_1 W]^T \hat{e}_k = W^T \hat{e}_j \cdot W^T \hat{e}_k = \sum_{i=1}^N (w_i \cdot \hat{e}_j)(w_i \cdot \hat{e}_k) = \sum_{i=1}^N Q_i \hat{e}_j \cdot \hat{e}_k = \sum_{i=1}^N X_1 Q_i \hat{e}_j \cdot \hat{e}_k. \quad (52)$$

This and equations (49) and (51) yield

$$F_{jk}(s) = \int_0^1 \frac{d\mu_{jk}(\lambda)}{s - \lambda}, \quad d\mu_{jk}(\lambda) = \sum_{i=1}^N \langle \delta_{\lambda_i}(d\lambda) X_1 Q_i \hat{e}_j \cdot \hat{e}_k \rangle. \quad (53)$$

This concludes our proof of Theorem 2

Corollary 2. *For each $\omega \in \Omega$, let $M(\omega) = W(\omega)\Lambda(\omega)W(\omega)$ be the eigenvalue decomposition of the real-symmetric matrix $M(\omega) = X_2(\omega)\Gamma_\bullet X_2(\omega)$. Here, the columns of the matrix $W(\omega)$ consist of the orthonormal eigenvectors $w_i(\omega)$, $i = 1, \dots, N$, of $M(\omega)$ and the diagonal matrix $\Lambda(\omega) = \text{diag}(\lambda_1(\omega), \dots, \lambda_N(\omega))$ involves its eigenvalues $\lambda_i(\omega)$. Denote $Q_i = w_i w_i^T$ the projection matrix onto the eigen-space spanned by w_i . The current field $J(\omega)$ satisfies $J(\omega) = J_0 + J_f(\omega)$, with $J_0 = \langle J(\omega) \rangle$ and $\Gamma_\bullet J(\omega) = J_f(\omega)$, and the effective complex resistivity tensor ρ^* has components ρ_{jk}^* , $j, k = 1, \dots, d$, which satisfy*

$$\rho_{jk}^* = \sigma_1^{-1}(\delta_{jk} - E_{jk}(s)), \quad E_{jk}(s) = \int_0^1 \frac{d\eta_{jk}(\lambda)}{s - \lambda}, \quad d\eta_{jk}(\lambda) = \sum_{i=1}^N \langle \delta_{\lambda_i}(d\lambda) X_2 Q_i \hat{e}_j \cdot \hat{e}_k \rangle. \quad (54)$$

C Projection method

In this section we provide a formulation for a numerically efficient *projection method* for computation of spectral measures and effective parameters for uniaxial polycrystalline media. Note that the sum inequation (53) runs only over the index set $i = 1, \dots, N_1$, as equation (50) implies that the masses $X_1 Q_i \hat{e}_j \cdot \hat{e}_k$ of the measure μ_{jk} are zero for $i = N_1 + 1, \dots, N$. Denote by λ_i^1 and w_i^1 , $i = 1, \dots, N_1$, the eigenvalues and eigenvectors of the $N_1 \times N_1$ matrix $\Gamma_1 = W_1 \Lambda_1 W_1^T$, defined in equation (47). Now, write

$$R \hat{e}_j = \begin{bmatrix} \hat{e}_j^{r_1} \\ \hat{e}_j^{r_2} \end{bmatrix}, \quad (55)$$

where $\hat{e}_j^{r_1} \in \mathbb{R}^{N_1}$ and $\hat{e}_j^{r_2} \in \mathbb{R}^{N_2}$. Therefore, writing the matrix $X_1 W$ in equation (50) in block diagonal form, $X_1 W = R^T \text{diag}(W_1, 0_{22})$, we have that

$$[X_1 W]^T \hat{e}_j \cdot [X_1 W]^T \hat{e}_k = [\text{diag}(W_1^T, 0_{22}) R \hat{e}_j] \cdot [\text{diag}(W_1^T, 0_{22}) R \hat{e}_k] = [W_1^T \hat{e}_j^{r_1}] \cdot [W_1^T \hat{e}_k^{r_1}]. \quad (56)$$

Denote by $Q_i^1 = w_i^1 [w_i^1]^T$, $i = 1, \dots, N_1$, the mutually orthogonal projection matrices, $Q_\ell^1 Q_m^1 = Q_\ell^1 \delta_{\ell m}$, onto the eigen-spaces spanned by the orthonormal eigenvectors w_i^1 . Equations (49), (51),

and (56) then yield

$$F_{jk}(s) = \langle (sI_1 - \Lambda_1)^{-1} [W_1^T \hat{e}_j^{r_1}] \cdot [W_1^T \hat{e}_k^{r_1}] \rangle = \left\langle \sum_{i=1}^{N_1} \frac{Q_i^1 \hat{e}_j^{r_1} \cdot \hat{e}_k^{r_1}}{s - \lambda_i^1} \right\rangle. \quad (57)$$

Equation (57) demonstrates that only the spectral information of the matrices W_1 and Λ_1 contribute to the functional representation for $F_{jk}(s)$ in (49) and its integral representation in (18). From a computational standpoint, this means that only the eigenvalues and eigenvectors of the $N_1 \times N_1$ matrix Γ_1 need to be computed in order to compute the spectral measures underlying the integral representations of the effective parameters for finite lattice systems. This is extremely cost effective as the numerical cost of finding all the eigenvalues and eigenvectors of a real-symmetric $N \times N$ matrix is $O(N^3)$ [43], so $N_1 = N/d$ implies the computational cost of the projection method is reduced by a factor of d^3 .

References

- [1] P. Anderson. Absence of diffusion in certain random lattices. *Phys. Rev.*, 109:1492–1505, 1958.
- [2] S. A. Arcone, A. J. Gow, and S. McGrew. Structure and dielectric properties at 4.8 and 9.5 GHz of saline ice. *J. Geophys. Res.*, 91(C12):14281–14303, 1986.
- [3] M. Avellaneda and A. Majda. Stieltjes integral representation and effective diffusivity bounds for turbulent transport. *Phys. Rev. Lett.*, 62:753–755, 1989.
- [4] M. Avellaneda and A. Majda. An integral representation and bounds on the effective diffusivity in passive advection by laminar and turbulent flow. *Comm. Math. Phys.*, 138:339–391, 1991.
- [5] M. Avellaneda and M. Vergassola. Stieltjes integral representation of effective diffusivities in time-dependent flows. *Phys. Rev. E*, 52(3):3249–3251, 1995.
- [6] G. A. Baker. *Quantitative Theory of Critical Phenomena*. Academic Press, New York, 1990.
- [7] G. A. Baker and P. R. Graves-Morris. *Padé Approximants*. Encyclopedia of Mathematics and its Applications. Cambridge University Press, 1996.
- [8] S. Barabash and D. Stroud. Spectral representation for the effective macroscopic response of a polycrystal: application to third-order non-linear susceptibility. *J. Phys., Condens. Matter*, 11:10323–10334, 1999.
- [9] H. F. Bates and L. H. Shapiro. Long-period gravity waves in ice-covered sea. *Journal of Geophysical Research*, 85(C2):1095, 1980.
- [10] A. Bensoussan, J. L. Lions, and G. Papanicolaou. *Asymptotic Analysis for Periodic Structures*. North-Holland, Amsterdam, The Netherlands, 1978.
- [11] D. J. Bergman. The dielectric constant of a composite material – A problem in classical physics. *Phys. Rep. C*, 43(9):377–407, 1978.
- [12] D. J. Bergman. Exactly solvable microscopic geometries and rigorous bounds for the complex dielectric constant of a two-component composite material. *Phys. Rev. Lett.*, 44:1285–1287, 1980.
- [13] D. J. Bergman. Rigorous bounds for the complex dielectric constant of a two-component composite. *Ann. Phys.*, 138:78, 1982.
- [14] D. J. Bergman and D. Stroud. Physical properties of macroscopically inhomogeneous media. *Solid State Phys.*, 46:147–269, 1992.
- [15] M. R. Beychok. *Fundamentals of Stack Gas Dispersion: Guide*. The Author, 1994.
- [16] R. Bhattacharya. Multiscale diffusion processes with periodic coefficients and an application to solute transport in porous media. *Ann. Appl. Probab.*, 9(4):951–1020, 1999.
- [17] L. Biferale, A. Crisanti, M. Vergassola, and A. Vulpiani. Eddy diffusivities in scalar transport. *Phys. of Fluids*, 7:2725–2734, 1995.

- [18] O. Bohigas and M. J. Giannoni. Chaotic motion and random matrix theories. In *Mathematical and computational methods in nuclear physics (Granada, 1983)*, volume 209 of *Lecture Notes in Physics*, pages 1–99. Springer, Berlin, 1984.
- [19] C. Bonifasi-Lista and E. Cherkaev. Analytical relations between effective material properties and microporosity: Application to bone mechanics. *International Journal of Engineering Science*, 46:1239–1252, 2008.
- [20] C. Bonifasi-Lista and E. Cherkaev. Electrical impedance spectroscopy as a potential tool for recovering bone porosity. *Phys. Med. Biol.*, 54(10):3063–3082, 2009.
- [21] C. Bonifasi-Lista, E. Cherkaev, and Y. N. Yeni. Analytical approach to recovering bone porosity from effective complex shear modulus. *Journal of Biomechanical Engineering*, 131(12), 2009.
- [22] S. R. Broadbent and J. M. Hammersley. Percolation processes I. Crystals and mazes. *Proc. Cambridge Philos. Soc.*, 53:629–641, 1957.
- [23] O. Bruno. The effective conductivity of strongly heterogeneous composites. *Proc. R. Soc. London A*, 433:353–381, 1991.
- [24] A. Bunde and S. Havlin, editors. *Fractals and Disordered Systems*. Springer-Verlag, New York, 1991.
- [25] C. M. Canali. Model for a random-matrix description of the energy-level statistics of disordered systems at the Anderson transition. *Phys. Rev. B*, 53(7):3713–3730, 1996.
- [26] J. T. Chayes and L. Chayes. Bulk transport properties and exponent inequalities for random resistor and flow networks. *Comm. Math. Phys.*, 105:133–152, 1986.
- [27] E. Cherkaev. Inverse homogenization for evaluation of effective properties of a mixture. *Inverse Problems*, 17(4):1203–1218, 2001.
- [28] E. Cherkaev. Spectral coupling of effective properties of a random mixture. In A. B. Movchan, editor, *IUTAM Symposium on Asymptotics, Singularities and Homogenisation in Problems of Mechanics*, volume 113 of *Solid Mechanics and Its Applications*, pages 331–340. Springer Netherlands, 2004.
- [29] E. Cherkaev. Internal friction and the Stieltjes analytic representation of the effective properties of two-dimensional viscoelastic composites. *Archive of Applied Mechanics*, 89(3):591–607, 2019.
- [30] E. Cherkaev. Internal resonances and relaxation memory kernels in composites. *Philosophical Transactions of the Royal Society A*, 378(2162):20190106, 2020.
- [31] E. Cherkaev and C. Bonifasi-Lista. Characterization of structure and properties of bone by spectral measure method. *J. Biomech.*, 44(2):345–351, 2011.
- [32] E. Cherkaev and K. M. Golden. Inverse bounds for microstructural parameters of composite media derived from complex permittivity measurements. *Waves in random media*, 8(4):437–450, 1998.
- [33] E. Cherkaev and M.-J. Ou. Dehomogenization: reconstruction of moments of the spectral measure of the composite. *Inverse Problems*, 24:065008 (19pp.), 2008.

- [34] E. Cherkaev and A. C. Tripp. Bounds on porosity for dielectric logging. In *9th Conference of the European Consortium for Mathematics in Industry*, pages 304–306. Technical University of Denmark, June 1996. Copenhagen, Denmark.
- [35] E. Cherkaev and D. Zhang. Coupling of the effective properties of a random mixture through the reconstructed spectral representation. *Physica B*, 338:16–23, 2003.
- [36] K. Christensen and N. R. Moloney. *Complexity and Criticality*. Imperial College Press, London, 2005.
- [37] J. P. Clerc, G. Giraud, J. M. Laugier, and J. M. Luck. The electrical conductivity of binary disordered systems, percolation clusters, fractals and related models. *Adv. Phys.*, 39(3):191–309, 1990.
- [38] G. T. Csanady. Turbulent diffusion of heavy particles in the atmosphere. *Journal of the Atmospheric Sciences*, 20(3):201–208, 1963.
- [39] A. R. Day, A. R. Grant, A. J. Sievers, and M. F. Thorpe. Spectral function of composites from reflectivity measurements. *Physical review letters*, 84(9):1978, 2000.
- [40] A. R. Day and M. F. Thorpe. The spectral function of random resistor networks. *J. Phys.: Cond. Matt.*, 8:4389–4409, 1996.
- [41] A. R. Day and M. F. Thorpe. The spectral function of composite - the inverse problem. *J. Phys. Condens. Matter*, 11:2551–2568, 1999.
- [42] P. Deift and D. Gioev. *Random Matrix Theory: Invariant Ensembles and Universality*. Courant Lecture Notes. Courant Institute of Mathematical Sciences, 2009.
- [43] J. W. Demmel. *Applied Numerical Linear Algebra*. SIAM, 1997.
- [44] E. Di Lorenzo, D. Mountain, H. P. Batchelder, N. Bond, and E. E. Hofmann. Advances in marine ecosystem dynamics from US GLOBEC: The horizontal-advection bottom-up forcing paradigm. *Oceanography*, 26(4):22–33, 2013.
- [45] H. Dinh, N. B. Murphy, E. Cherkaev, C. Strong, and K. M. Golden. Anomalous diffusion and transport in sea ice dynamics. 11 pp., Preprint, 2022.
- [46] A. L. Efros and B. I. Shklovskii. Critical behavior of conductivity and dielectric constant near the metal-non-metal transition threshold. *Phys. Stat. Sol. (b)*, 76:475–485, 1976.
- [47] C. Engström. Bounds on the effective tensor and the structural parameters for anisotropic two-phase composite material. *Journal of Physics D: Applied Physics*, 38(19):3695, 2005.
- [48] F. Evers and A. D. Mirlin. Anderson transitions. *Rev. Modern Phys.*, 80(4):1355–1418, 2008.
- [49] A. Fannjiang and G. Papanicolaou. Convection enhanced diffusion for periodic flows. *SIAM J. Appl. Math.*, 54(2):333–408, 1994.
- [50] A. Fannjiang and G. Papanicolaou. Convection-enhanced diffusion for random flows. *J. Stat. Phys.*, 88(5-6):1033–1076, 1997.
- [51] A. C. Fannjiang. Phase diagram for turbulent transport: sampling drift, eddy diffusivity, and variational principles. *Physica. D, Nonlinear phenomena*, 136:145–174, 2000.

- [52] S. Feng, B. I. Halperin, and P. N. Sen. Transport properties of continuum systems near the percolation threshold. *Phys. Rev. B*, 35:197–214, 1987.
- [53] K. Golden. Bounds on the complex permittivity of a multicomponent material. *J. Mech. Phys. Solids*, 34(4):333–358, 1986.
- [54] K. Golden. Convexity and exponent inequalities for conduction near percolation. *Phys. Rev. Lett.*, 65(24):2923–2926, 1990.
- [55] K. Golden. Bounds on the complex permittivity of sea ice. *J. Geophys. Res. (Oceans)*, 100(C7):13,699 – 13,711, 1995.
- [56] K. Golden and G. Papanicolaou. Bounds for effective parameters of heterogeneous media by analytic continuation. *Comm. Math. Phys.*, 90:473–491, 1983.
- [57] K. Golden and G. Papanicolaou. Bounds for effective parameters of multicomponent media by analytic continuation. *J. Stat. Phys.*, 40(5/6):655–667, 1985.
- [58] K. M. Golden. Exponent inequalities for the bulk conductivity of a hierarchical model. *Comm. Math. Phys.*, 43(3):467–499, 1992.
- [59] K. M. Golden. Critical behavior of transport in lattice and continuum percolation models. *Phys. Rev. Lett.*, 78(20):3935–3938, 1997.
- [60] K. M. Golden. The interaction of microwaves with sea ice. In G. Papanicolaou, editor, *Wave Propagation in Complex Media, IMA Volumes in Mathematics and its Applications, Vol. 96*, pages 75 – 94. Springer – Verlag, 1997.
- [61] K. M. Golden. Percolation models for porous media. In U. Hornung, editor, *Homogenization and Porous Media*, pages 27 – 43. Springer – Verlag, 1997.
- [62] K. M. Golden. Climate change and the mathematics of transport in sea ice. *Notices of the American Mathematical Society*, 56(5):562–584 and issue cover, 2009.
- [63] K. M. Golden. Mathematics of sea ice. In N. J. Higham, M. R. Dennis, P. Glendinning, P. A. Martin, F. Santosa, and J. Tanner, editors, *The Princeton Companion to Applied Mathematics*, pages 694–705. Princeton University Press, Princeton, 2015.
- [64] K. M. Golden and S. F. Ackley. Modeling of anisotropic electromagnetic reflection from sea ice. *J. Geophys. Res. (Oceans)*, 86(C9):8107–8116, 1981.
- [65] K. M. Golden, S. F. Ackley, and V. I. Lytle. The percolation phase transition in sea ice. *Science*, 282:2238–2241, 1998.
- [66] K. M. Golden, L. G. Bennetts, E. Cherkaev, I. Eisenman, D. Feltham, C. Horvat, E. Hunke, C. Jones, D. Perovich, P. Ponte-Castañeda, C. Strong, D. Sulsky, and A. Wells. Modeling sea ice. *Notices of the American Mathematical Society*, 67(10):1535–1555 and issue cover, 2020.
- [67] K. M. Golden, D. Borup, M. Cheney, E. Cherkaeva, M. S. Dawson, K. H. Ding, A. K. Fung, D. Isaacson, S. A. Johnson, , A. K. Jordan, J. A. Kong, R. Kwok, S. V. Nghiem, R. G. Onstott, J. Sylvester, D. P. Winebrenner, and I. Zabel. Inverse electromagnetic scattering models for sea ice. *IEEE Trans. Geosci. Rem. Sens.*, 36(5):1675–1704, 1998.

- [68] K. M. Golden, M. Cheney, K. H. Ding, A. K. Fung, T. C. Grenfell, D. Isaacson, J. A. Kong, S. V. Nghiem, J. Sylvester, and D. P. Winebrenner. Forward electromagnetic scattering models for sea ice. *IEEE Trans. Geosci. Rem. Sens.*, 36(5):1655–1674, 1998.
- [69] K. M. Golden, H. Eicken, A. L. Heaton, J. Miner, D. Pringle, and J. Zhu. Thermal evolution of permeability and microstructure in sea ice. *Geophys. Res. Lett.*, 34:L16501 (6 pages and issue cover), 2007.
- [70] K. M. Golden, N. B. Murphy, and E. Cherkaev. Spectral analysis and connectivity of porous microstructures in bone. *J. Biomech.*, 44(2):337–344, 2011.
- [71] K. M. Golden, C. S. Sampson, A. Gully, D. J. Lubbers, and J.-L. Tison. Percolation threshold for bulk fluid flow through Antarctic granular sea ice. 12 pp., Preprint, 2022.
- [72] G. Grimmett. *Percolation*. Springer-Verlag, New York, 1989.
- [73] T. Guhr, A. Müller-Groeling, and H. A. Weidenmüller. Random-matrix theories in quantum physics: Common concepts. *Phys. Rept.*, 299(4–6):189–425, June 1998.
- [74] A. Gully, L. G. E. Backstrom, H. Eicken, and K. M. Golden. Complex bounds and microstructural recovery from measurements of sea ice permittivity. *Physica B*, 394:357–362, 2007.
- [75] A. Gully, J. Lin, E. Cherkaev, and K. M. Golden. Bounds on the complex permittivity of polycrystalline composites by analytic continuation. *Proceedings of the Royal Society A: Mathematical and Physical Sciences*, 471(2174):20140702 and issue cover, 2015.
- [76] B. I. Halperin, S. Feng, and P. N. Sen. Differences between lattice and continuum percolation transport exponents. *Phys. Rev. Lett.*, 54(22):2391–2394, 1985.
- [77] Z. Hashin and S. Shtrikman. A variational approach to the theory of effective magnetic permeability of multiphase materials. *J. Appl. Phys.*, 33:3125–3131, 1962.
- [78] E. E. Hofmann and E. J. Murphy. Advection, krill, and Antarctic marine ecosystems. *Antarct. Sci.*, 16(04):487–499, 12 2004.
- [79] C. Hohenegger, B. Alali, K. R. Steffen, D. K. Perovich, and K. M. Golden. Transition in the fractal geometry of Arctic melt ponds. *The Cryosphere*, 6(5):1157–1162, 2012.
- [80] R. A. Horn and C. R. Johnson. *Matrix Analysis*. Cambridge University Press, 1990.
- [81] Tsung-Ming Huang, Wen-Wei Lin, and Weichung Wang. Matrix representations of discrete differential operators and operations in electromagnetism. *Ann. Math. Sci. Appl.*, 4(1):55–79, 2019.
- [82] T. Jonckheere and J. M. Luck. Dielectric resonances of binary random networks. *J. Phys. A: Math. Gen.*, 31:3687–3717, 1998.
- [83] J. Kabel, A. Odgaard, B. van Rietbergen, and R. Huiskes. Connectivity and the elastic properties of cancellous bone. *Bone*, 24(2):115–120, 1999.
- [84] J. B. Keller. Gravity waves on ice-covered water. *Journal of Geophysical Research: Oceans*, 103(C4):7663–7669, apr 1998.

- [85] A. R. Kerstein. Equivalence of the void percolation problem for overlapping spheres and a network problem. *J. Phys. A*, 16:3071–3075, 1983.
- [86] S. M. Kozlov. Geometric aspects of homogenization. *Russ. Math. Surv.*, 44:91, 1989.
- [87] N. Kraitzman, R. Hardenbrook, H. Dinh, N. B. Murphy, E. Cherkaev, J. Zhu, and K. M. Golden. Bounds on convection enhanced thermal transport in sea ice. Preprint, 2022.
- [88] V. E. Kravtsov and K. A. Muttalib. New class of random matrix ensembles with multifractal eigenvectors. *Phys. Rev. Lett.*, 79(10):1913–1916, 1997.
- [89] O. Levy and E. Cherkaev. Effective medium approximations for anisotropic composites with arbitrary component orientation. *Journal of Applied Physics*, 114(16):164102, 2013.
- [90] J. Li, A. V. Babanin, Q. Liu, J. J. Voermans, P. Heil, and Y. Tang. Effects of wave-induced sea ice break-up and mixing in a high-resolution coupled ice-ocean model. *Journal of Marine Science and Engineering*, 9(4), 2021.
- [91] J. V. Lukovich, J. K. Hutchings, and D. G. Barber. On sea-ice dynamical regimes in the Arctic Ocean. *Ann. Glac.*, 56(69):323–331, 2015.
- [92] V. I. Lytle and S. F. Ackley. Heat flux through sea ice in the Western Weddell Sea: Convective and conductive transfer processes. *J. Geophys. Res.*, 101(C4):8853–8868, 1996.
- [93] A. J. Majda and P. R. Kramer. *Simplified Models for Turbulent Diffusion: Theory, Numerical Modelling, and Physical Phenomena*. Physics Reports. North-Holland, 1999.
- [94] A. J. Majda and P. E. Souganidis. Large scale front dynamics for turbulent reaction-diffusion equations with separated velocity scales. *Nonlinearity (Bristol)*, 7(1):1–30, 1994.
- [95] J. A. Maslanik, C. Fowler, J. Stroeve, S. Drobot, J. Zwally, D. Yi, and W. Emery. A younger, thinner Arctic ice cover: Increased potential for rapid, extensive sea-ice loss. *Geophys. Res. Lett.*, 34:L24501, doi:10.1029/2007GL032043, 2007.
- [96] D. McLaughlin, G. Papanicolaou, and O. Pironneau. Convection of microstructure and related problems. *SIAM J. Appl. Math.*, 45:780–797, 1985.
- [97] K. McLean, E. Cherkaev, and K. M. Golden. Bounds on the complex permittivity of polycrystalline sea ice with anisotropy in the horizontal plane. In preparation, 2022.
- [98] R. C. McPhedran, D. R. McKenzie, and G. W. Milton. Extraction of structural information from measured transport properties of composites. *Applied Physics A: Materials Science & Processing*, 29(1):19–27, 1982.
- [99] R. C. McPhedran and G. W. Milton. Inverse transport problems for composite media. *MRS Proceedings*, 195, 1 1990.
- [100] G. W. Milton. Bounds on the complex dielectric constant of a composite material. *Appl. Phys. Lett.*, 37:300–302, 1980.
- [101] G. W. Milton. Bounds on the complex permittivity of a two-component composite material. *J. Appl. Phys.*, 52:5286–5293, 1981.
- [102] G. W. Milton. *Theory of Composites*. Cambridge University Press, Cambridge, 2002.

- [103] Graeme W Milton. Universal bounds on the electrical and elastic response of two-phase bodies and their application to bounding the volume fraction from boundary measurements. *Journal of the Mechanics and Physics of Solids*, 60(1):139–155, 2012.
- [104] H. K. Moffatt. Transport effects associated with turbulence with particular attention to the influence of helicity. *Rep. Prog. Phys.*, 46(5):621–664, 1983.
- [105] D. Morison, N. B. Murphy, E. Cherkaev, and K. M. Golden. Order to disorder in quasiperiodic composites. *Communications Physics*, 5(148):9 pp., 2022.
- [106] J. E. M. Mosig, F. Montiel, and V. A. Squire. Comparison of viscoelastic-type models for ocean wave attenuation in ice-covered seas. *Journal of Geophysical Research: Oceans*, 120(9):6072–6090, sep 2015.
- [107] N. B. Murphy, E. Cherkaev, and K. M. Golden. Anderson transition for classical transport in composite materials. *Phys. Rev. Lett.*, 118:036401, 2017.
- [108] N. B. Murphy, E. Cherkaev, C. Hohenegger, and K. M. Golden. Spectral measure computations for composite materials. *Commun. Math. Sci.*, 13(4):825–862, 2015.
- [109] N. B. Murphy, E. Cherkaev, J. Xin, and K. M. Golden. Spectral measures and iterative bounds for effective diffusivity for periodic flows. In Preparation, 2022.
- [110] N. B. Murphy, E. Cherkaev, J. Xin, J. Zhu, and K. M. Golden. Spectral analysis and computation of effective diffusivities in space-time periodic incompressible flows. *Ann. Math. Sci. Appl.*, 2(1):3–66, 2017.
- [111] N. B. Murphy, E. Cherkaev, J. Zhu, J. Xin, and K. M. Golden. Spectral analysis and computation for homogenization of advection diffusion processes in steady flows. *J. Math. Phys.*, 61:013102, 34 pp., 2020.
- [112] N. B. Murphy and K. M. Golden. The Ising model and critical behavior of transport in binary composite media. *J. Math. Phys.*, 53:063506 (25pp.), 2012.
- [113] D. Notz and SIMIP Community. Arctic sea ice in CMIP6. *Geophysical Research Letters*, 47(10):e2019GL086749, 2020.
- [114] D. Notz and J. Stroeve. Observed Arctic sea-ice loss directly follows anthropogenic CO₂ emission. *Science*, 354(6313):747–750, 2016.
- [115] C. Orum, E. Cherkaev, and K. M. Golden. Recovery of inclusion separations in strongly heterogeneous composites from effective property measurements. *Proc. Roy. Soc. London A*, 468(2139):784–809, 2012.
- [116] G. Papanicolaou and S. Varadhan. Boundary value problems with rapidly oscillating coefficients. In *Colloquia Mathematica Societatis János Bolyai 27, Random Fields (Esztergom, Hungary 1979)*, page 835. North-Holland, 1982.
- [117] G. A. Pavliotis. *Homogenization theory for advection-diffusion equations with mean flow*. PhD thesis, Rensselaer Polytechnic Institute Troy, New York, 2002.
- [118] G. A. Pavliotis. Asymptotic analysis of the Green–Kubo formula. *IMA J. Appl. Math.*, 75:951–967, 2010.

- [119] C. Petrich and H. Eicken. Growth, structure and properties of sea ice. In D. N. Thomas and G. S. Dieckmann, editors, *Sea Ice*, pages 23–77. Wiley-Blackwell, 2009.
- [120] V. Plerou, P. Gopikrishnan, B. Rosenow, L. A. N. Amaral, T. Guhr, and H. E. Stanley. Random matrix approach to cross correlations in financial data. *Phys. Rev. E*, 65(6):066126, June 2002.
- [121] J. R. Reimer, F. R. Adler, K. M. Golden, and A. Narayan. Uncertainty quantification for ecological models with random parameters. *Ecology Letters*, 25(10):2232–2244, 2022.
- [122] M. Sahimi. *Applications of Percolation Theory*. Taylor and Francis Ltd., London, 1994.
- [123] M. Sahimi. *Flow and Transport in Porous Media and Fractured Rock*. VCH, Weinheim, 1995.
- [124] C. S. Sampson, N. B. Murphy, E. Cherkaev, and K. M. Golden. Bounds on the complex viscoelasticity for surface waves on ice-covered seas. 12 pp., Preprint, 2022.
- [125] P. J. Samson. Atmospheric transport and dispersion of air pollutants associated with vehicular emissions. In A. Y. Watson, R. R. Bates, and D. Kennedy, editors, *Air Pollution, the Automobile, and Public Health*, pages 77–97. National Academy Press (US), 1988.
- [126] B. I. Shklovskii, B. Shapiro, B. R. Sears, P. Lambrianides, and H. B. Shore. Statistics of spectra of disordered systems near the metal-insulator transition. *Phys. Rev. B*, 47(17):11,487–11,490, 1993.
- [127] D. Stauffer and A. Aharony. *Introduction to Percolation Theory, Second Edition*. Taylor and Francis Ltd., London, 1992.
- [128] A. D. Stone, P. A. Mello, K. A. Muttalib, and J.-L. Pichard. *Random Matrix Theory and Maximum Entropy Models for Disordered Conductors*, chapter 9, pages 369–448. Elsevier Science Publishers, Amsterdam, Netherlands, 1991.
- [129] J. Stroeve, M. M. Holland, W. Meier, T. Scambos, and M. Serreze. Arctic sea ice decline: Faster than forecast. *Geophysical Research Letters*, 34(9):L09501, 2007.
- [130] J. C. Stroeve, V. Kattsov, A. Barrett, M. Serreze, T. Pavlova, M. Holland, and W. N. Meier. Trends in Arctic sea ice extent from CMIP5, CMIP3 and observations. *Geophysical Research Letters*, 39:L16502, 2012.
- [131] C. Strong and I. G. Rigor. Arctic marginal ice zone trending wider in summer and narrower in winter. *Geophys. Res. Lett.*, 40(18), 2013.
- [132] G. I. Taylor. Diffusion by continuous movements. *Proceedings of the London Mathematical Society. Third Series*, 2:196–211, 1921.
- [133] Andrew E Thaler and Graeme W Milton. Exact determination of the volume of an inclusion in a body having constant shear modulus. *Inverse Problems*, 30(12):125008, 2014.
- [134] D. N. Thomas and G. S. Dieckmann, editors. *Sea Ice: An Introduction to its Physics, Chemistry, Biology and Geology*. Blackwell, Oxford, 2003.
- [135] C. J. Thompson. *Classical Equilibrium Statistical Mechanics*. Oxford University Press, Oxford, 1988.

- [136] S. Torquato. *Random Heterogeneous Materials: Microstructure and Macroscopic Properties*. Springer-Verlag, New York, 2002.
- [137] A. C. Tripp, E. Cherkaev, and J. Hulén. Bounds on the complex conductivity of geophysical mixtures. *Geophysical Prospecting*, 46(6):589–601, 1998.
- [138] J. Turner, C. Holmes, T. C. Harrison, T. Phillips, B. Jena, T. Reeves-Francois, R. Fogt, E. R. Thomas, and C. C. Bajish. Record low Antarctic sea ice cover in February 2022. *Geophysical Research Letters*, 49(12):e2022GL098904, 2022.
- [139] N. Untersteiner. *The Geophysics of Sea Ice*. Plenum, New York, 1986.
- [140] R. Wang and H. H. Shen. Gravity waves propagating into an ice-covered ocean: A viscoelastic model. *Journal of Geophysical Research*, 115(C6), June 2010.
- [141] T. Waseda, A. Webb, K. Sato, J. Inoue, A. Cohout, B. Penrose, and S. Penrose. Correlated increase of high ocean waves and winds in the ice-free waters of the arctic ocean. *Sci. Rep.*, 8:4489, 2018.
- [142] W. M. Washington and C. L. Parkinson. *An Introduction to Three-Dimensional Climate Modeling*. University Science Books, 1986.
- [143] E. Watanabe and H. Hasumi. Pacific water transport in the western Arctic Ocean simulated by an eddy-resolving coupled sea ice–ocean model. *J. Phys. Oceanogr.*, 39(9):2194–2211, 2009.
- [144] W. F. Weeks and S. F. Ackley. The growth, structure and properties of sea ice. Monograph 82-1, USA CRREL, Hanover, NH, 1982.
- [145] W. F. Weeks and A. J. Gow. Crystal alignments in the fast ice of Arctic Alaska. *J. Geophys. Res.*, 85(C2):1137–1146, 1980.
- [146] M. G. Worster and D. W. Rees Jones. Sea-ice thermodynamics and brine drainage. *Philos. Trans. Royal Soc. A*, 373:20140166, 2015.
- [147] J. Xin. *An Introduction to Fronts in Random Media*. Surveys and Tutorials in the Applied Mathematical Sciences. Springer New York, 2009.
- [148] D. Zhang and E. Cherkaev. Reconstruction of spectral function from effective permittivity of a composite material using rational function approximations. *J. Comput. Phys.*, 228(15):5390–5409, 2009.